

 Open access • Posted Content • DOI:10.1101/2021.06.03.446920

## Identifying developing interneurons as a potential target for multiple genetic autism risk factors in human and rodent forebrain. — [Source link](#)

Yifei Yang, Sam A. Booker, James M. Clegg, Idoia Quintana-Urzaiz ...+8 more authors

**Institutions:** University of Edinburgh, University of Strasbourg

**Published on:** 03 Jun 2021 - bioRxiv (Cold Spring Harbor Laboratory)

**Topics:** Autism and Axon initial segment

Related papers:

- [Identification of Vulnerable Cell Types in Major Brain Disorders Using Single Cell Transcriptomes and Expression Weighted Cell Type Enrichment.](#)
- [Transcriptome analysis reveals dysregulation of innate immune response genes and neuronal activity-dependent genes in autism.](#)
- [Sex-biased gene expression in the developing brain: implications for autism spectrum disorders.](#)
- [Atypical neurogenesis and excitatory-inhibitory progenitor generation in induced pluripotent stem cell \(iPSC\) from autistic individuals](#)
- [Cell-Type-Specific Analysis of Molecular Pathology in Autism Identifies Common Genes and Pathways Affected Across Neocortical Regions](#)

Share this paper:    

View more about this paper here: <https://typeset.io/papers/identifying-developing-interneurons-as-a-potential-target-2h3od8cl7o>

1 **TITLE**

2 **Identifying developing interneurons as a potential target for multiple genetic**  
3 **autism risk factors in human and rodent forebrain.**

4

5 **AUTHORS/AFFILIATIONS**

6 **Yifei Yang<sup>1,2</sup>, Sam A. Booker<sup>1,2</sup>, James M. Clegg<sup>1,2</sup>, Idoia Quintana Urzainqui<sup>1,2</sup>,**  
7 **Anna Sumera<sup>1,2</sup>, Zrinko Kozic<sup>1,2</sup>, Owen Dando<sup>1,2</sup>, Sandra Martin Lorenzo<sup>3</sup>, Yann**  
8 **Herault<sup>3</sup>, Peter C. Kind<sup>1,2</sup>, David J. Price<sup>1,2</sup>, Thomas Pratt<sup>1,2</sup>, \***

9 <sup>1</sup>Simons Initiative for the Developing Brain,

10 <sup>2</sup>Centre for Discovery Brain Sciences,

11 Hugh Robson Building, Edinburgh Medical School Biomedical Sciences,

12 The University of Edinburgh, Edinburgh, EH8 9XD, United Kingdom.

13 <sup>3</sup>Université de Strasbourg, CNRS, INSERM, Institut de Génétique et de Biologie

14 Moléculaire et Cellulaire, IGBMC, 1 rue Laurent Fries, 67404 Illkirch, France

15

16 **CONTACT INFO**

17 \*Correspondence : [t.pratt@ed.ac.uk](mailto:t.pratt@ed.ac.uk)

18

19 **ABSTRACT**

20 Autism spectrum condition or ‘autism’ is associated with numerous monogenic and  
21 polygenic genetic risk factors including the polygenic *16p11.2* microdeletion. A central  
22 question is what neural cells are affected. To systematically investigate we analysed  
23 single cell transcriptomes from gestational week (GW) 8-26 human foetal prefrontal  
24 cortex and identified a subset of interneurons (INs) first appearing at GW23 with  
25 enriched expression of a disproportionately large fraction of risk factor transcripts. This  
26 suggests the hypothesis that these INs are disproportionately vulnerable to mutations  
27 causing autism. We investigated this in a rat model of the *16p11.2* microdeletion. We  
28 found no change in the numbers or position of either excitatory or inhibitory neurons  
29 in the somatosensory cortex or CA1 of *16p11.2*<sup>+/-</sup> rats but found that CA1 Sst INs were  
30 hyperexcitable with an enlarged axon initial segment, which was not the case for CA1

31 pyramidal cells. This study prompts deeper investigation of IN development as a  
32 convergent target for autism genetic risk factors.

33

## 34 **KEYWORDS**

35 Development, telencephalon, autism, genetics, *16p11.2*, GABAergic, human, rat,  
36 electrophysiology, AIS.

37

38 Contributions and acknowledgements: YY and IQ performed bioinformatic analysis of  
39 human data, SAB, JMC, and AS performed rat experiments and analysis, ZK and OD  
40 contributed to linear modelling, SM and YH provided the *16p11.2* microdeletion rats,  
41 PCK and DJP contributed to design, TP designed the study and wrote the paper. This  
42 work was funded by the Simons Initiative for the Developing Brain (SFARI - 529085)  
43 and Biotechnology and Biological Sciences Research Council (BB/M00693X/1).

44

## 45 **INTRODUCTION**

46 Autism spectrum conditions (ASC – referred to here as ‘autism’) describe several  
47 symptoms and behaviours which affect the way in which a group of people understand  
48 and react to the world around them (Mental Health Foundation) and may co-occur with  
49 other conditions including epilepsy and intellectual disability (ID). Recent efforts to  
50 understand the genetic landscape of autism identified hundreds of genetic risk factors  
51 predisposing to autism including *de novo* single gene mutation (5-10%), copy number  
52 variations (CNVs) and chromosome anomalies (5%), and inherited single gene  
53 mutations (3%), although most cases (80-85%) have no known genetic cause.

54 Genetic risk factors can be either ‘monogenic’ where a single gene mutation is  
55 sufficient to predispose to autism or ‘polygenic’ where one mutation directly affects  
56 several genes simultaneously. CNVs are an example of the latter where chromosomal  
57 microduplication or microdeletion affect the gene dosage of multiple genes. The  
58 Simons Foundation Autism Research Initiative (SFARI) curates a list of ~1000  
59 monogenic genetic risk factors of which 83 are categorised as the highest ranking  
60 (Categories 1 ‘high confidence’ and 2 ‘strong candidates’) indicating a robust

61 association between mutation in these genes and autism. SFARI lists 2240 CNVs  
62 associated with autism of which *16p11.2* microdeletion and microduplication are  
63 among the most frequent accounting for approximately 1% of cases. The *16p11.2*  
64 CNV comprises 27 protein coding genes so is a polygenic risk factor although it is  
65 currently unknown the extent to which each of the *16p11.2* genes are individual risk  
66 factors.

67 Autism manifests in early infancy and then persists into later life. A number of lines of  
68 evidence suggest that events during brain development *in utero* contribute to the  
69 subsequent development of symptoms (Packer, 2016). The developing cerebral  
70 cortex is comprised of three neuronal cardinal cell classes (progenitors, excitatory  
71 neurons, and inhibitory neurons) and three non-neuronal cardinal cell classes  
72 (astrocytes, oligodendrocyte precursors, and microglia). One important factor for  
73 cerebral cortex function is the balance between glutamatergic, excitatory principal  
74 neurons, which originate from progenitors located in the ventricular zone of the  
75 cerebral cortex, and inhibitory GABAergic interneurons (INs) which originate from  
76 progenitors located in the ganglionic eminences and then migrate into the cortex and  
77 integrate within functional circuits of the cortical plate (Hansen et al., 2013; Ma et al.,  
78 2013). Changes in the number, position, anatomy, or electrophysiology of inhibitory or  
79 excitatory neurons may perturb the excitatory/inhibitory balance (the E/I balance) and  
80 is hypothesised to be a convergent mechanism in autism and its co-occurring  
81 conditions (Bozzi et al., 2018; Nelson and Valakh, 2015; Puts et al., 2017; Rapanelli  
82 et al., 2017; Robertson et al., 2016) (Antoine et al., 2019)

83 The aim of the current study is to systematically identify types of cell in developing  
84 human cerebral cortex that are potentially vulnerable to autism risk factors using a  
85 single cell mRNA sequencing (scRNA-seq) dataset acquired from developing human  
86 foetal cortex spanning gestational weeks (GW) 8 to 26 (Zhong et al., 2018). While we  
87 found that some autism associated transcripts are differentially expressed between  
88 the cardinal cell classes our most striking finding was that a subset of differentiating  
89 INs first appearing at GW23 exhibited enriched expression of a strikingly high  
90 proportion of risk transcripts. This molecular analysis suggests the hypothesis that a  
91 large number of monogenic risk factors and the polygenic *16p11.2* microdeletion  
92 selectively target IN development resulting in IN phenotypes postnatally that contribute  
93 to autism and its comorbid conditions. We support this hypothesis using a *16p11.2*

94 microdeletion rat model where we identified hypersensitive electrophysiology and  
95 enlarged axon initial segment (AIS) phenotypes in somatostatin (Sst) expressing  
96 hippocampal INs.

97

## 98 **METHODS.**

### 99 **Datasets**

100 Three published cortical transcriptome datasets were used in this study to explore the  
101 gene expression pattern of autism-associated genes during cortical development.

102 The raw gene expression matrix in the scRNA-seq data of human foetal PFC was  
103 obtained from the Gene Expression Omnibus (GEO) under the accession number  
104 GSE104276, then the data was normalized as the original paper described (Zhong et  
105 al., 2018). We used the authors' original classification of six cardinal cell classes (NPC,  
106 ExN, IN, OPC, Astrocyte and Microglia).

107 The expression matrix of genes in the adult human cortical single nuclei RNA-seq data  
108 were downloaded under the accession number of GSE97930 (Lake et al., 2018). In  
109 the dataset from Lake et al., only cells that identified as "INs" were used for further  
110 analysis. The original eight interneuron clusters were grouped based on the  
111 expression pattern of marker genes (In1/2/3 as VIP, In4 as NG, In6 as PV, In7/8 as  
112 SST, Figure 2B,C in Lake et al., 2018).

113 For the mouse scRNA-seq datasets at of *Dlx6a-cre* fate-mapped cortical inhibitory  
114 neurons, the pre-processed Seurat objects were downloaded from the author's share  
115 link ([https://www.dropbox.com/s/qe2carqnf9eu4sd/Filtered\\_Mayer-et-  
116 al.Rda.zip?dl=0](https://www.dropbox.com/s/qe2carqnf9eu4sd/Filtered_Mayer-et-al.Rda.zip?dl=0)) (Mayer et al., 2018). We used the authors' original classification of  
117 seven IN cell types (Sst, Pvalb, Vip, Id2, Nos1, Th and Igfbp6).

118 All three datasets were converted into Seurat objects by R package Seurat (version  
119 2.3.0) for further analysis. In detail, in the dataset from Zhong et al., raw read counts  
120 were normalized based on the original paper described. Any cells with less than 1000  
121 genes expressed were removed, and any gene expressed by less than 3 cells at less  
122 than 1 normalized expression value was removed. Pseudogenes, miRNA, rRNA,  
123 mitochondrial associated and ribosome related genes were excluded from further

124 analysis. The filtered gene expression matrix and the classification of the cardinal cell  
125 classes were used to create a Seurat object. We also create a Seurat object for the  
126 dataset from Lake et al. using the same procedure. The pre-processed Seurat object  
127 from Mayer et al was not changed. The scRNA-Seq data was also analyzed with  
128 BBrowser version 2.2.44 (SingleCell).

### 129 **Lists of autism risk genes**

130 Monogenic autism associated genes were downloaded from the SFARI database  
131 (released May 2019) (<https://gene.sfari.org/database/human-gene/>) and the 83  
132 highest ranking (SFARI 1+2) were analysed as these genes are significant statistically  
133 in genome-wide studies between cases and controls. Besides these monogenetic  
134 genes, the copy number variance (CNV) of genetic loci (CNV genes), either deletions  
135 or duplications, are also linked to autism. We selected the 27 protein coding genes at  
136 the *16p11.2* locus since both duplication and deletion of these genes has been linked  
137 to significantly increased incidence of autism representing a potentially polygenic  
138 cause of autism.

### 139 **Clustering and visualization of cell types**

140 The identification of six cardinal cell classes were obtained from the original paper and  
141 re-plotted in a two-dimensional space of t-Distributed Stochastic Neighbor Embedding  
142 (tSNE). In details, the highly variable genes (HVGs) were identified using Seurat  
143 function FindVariableGenes. The mean of logged expression values was plotted  
144 against variance to mean expression level ratio (VMR) for each gene. Genes with log  
145 transformed mean expression level between 1 and 8, and VMR lower than 1.2 were  
146 considered as highly variable genes. Then principal component analysis (PCA) was  
147 performed with RunPCA function in Seurat using HVGs to analyze all the cells.  
148 Following the PCA, we conducted JACKSTRAW analysis with 100 iterations to identify  
149 statistically significant ( $p$  value  $< 0.01$ ) principal components (PCs) that were driving  
150 systematic variation. We used tSNE to present data in two-dimensional coordinates,  
151 generated by RunTSNE function in Seurat, and the first 7 significant PCs identified by  
152 JACKSTRAW analysis were used as input to RunTSNE function. Perplexity was set  
153 to 20. t-SNE plot and the violin plot were generated using R package ggplot2.

154 We further clustered the three cardinal cell classes (NPC, ExN and IN) from the foetal  
155 cortical dataset. Due to the different number of cells and the variant gene expression

156 pattern in each cardinal cell class, the HVGs were identified using the same method  
157 but with the different parameters. For the cells in NPC, genes with log transformed  
158 mean expression level between 0.5 and 8, and VMR lower than 1.2 were considered  
159 as highly variable genes. For the cells in ExN and IN classes, genes with log  
160 transformed mean expression level between 1 and 10, and VMR lower than 0.5 were  
161 considered as highly variable genes. Then the statistically significant PCs were  
162 calculated by JACKSTRAW analysis and used as input to get tSNE coordinates.  
163 Clustering was done with Luvain Jaccard algorithm using t-SNE coordinates by  
164 FindClusters function from Seurat. The resolution parameters used to IDENTIFY  
165 clusters within the three cardinal cell classes were: NPC, resolution = 1; ExN,  
166 resolution = 0.1; and IN, resolution = 0.5. Other parameters that we left at default.

### 167 **Identification of differential expressed genes**

168 All differential expression (DE) analyses were conducted using Seurat function  
169 *FindAllMarkers*. In brief, we took one group of cells and compared it with the rest of  
170 the cells, using Wilcoxon rank sum test. For any given comparison we only considered  
171 genes that were expressed by at least 33% of cells in either population. Genes that  
172 exhibit p values under 0.05, as well as log fold change over 0.33 were considered  
173 significant. All heatmaps of DE analysis were plotted using R package pheatmap  
174 (Figure 1C, Figure 3A and 3B, and Figure 5D).

### 175 **MetaNeighbor analysis**

176 MetaNeighbor analysis was performed using the R function MetaNeighbor with default  
177 settings (Crow et al., 2018). The AUROC (Area under the Receiver Operating  
178 Characteristic) scores produced by MetaNeighbor analysis indicate the degree of  
179 correlation between cell clusters. Three gene lists were used as input to do  
180 MetaNeighbor analysis among the 21 clusters of human foetal dataset: Highly variable  
181 genes (HVGs) identified as significant differentially expressed genes (DEGs) between  
182 the clusters (Figure S2A); monogenic autism risk genes (Figure S2B); and *16p11.2*  
183 genes (Figure S2C). The results from the MetaNeighbor analysis were plotted as a  
184 heatmap using the gplots function heatmap. For a given gene set each pairwise  
185 comparison between cell clusters is given an AUROC score ranging from 1.0 (red on  
186 the heatmap) indicating that cells were highly probable to be of the same type to 0.0  
187 (blue on the heatmap) indicating that it was highly improbable that the cells were of

188 the same type. A score on 0.5 (yellow on the heatmap) indicates that the gene set  
189 used was unable to distinguish between the cells better than by chance.

## 190 **Projection based on multiple datasets**

191 We conducted canonical correlation analysis (CCA) and *k*-nearest neighbors analysis  
192 (KNN) as we previous described to classify the cell types of foetal INs based on the  
193 cell type features in the adult transcriptomics datasets (Mi et al., 2018). Briefly, we first  
194 performed random forest analysis within HVGs to do feature selection for both foetal  
195 and adult human cortical INs. Then we selected the shared HVGs between two  
196 datasets that best represented the feature of IN cell types. The HVGs were used as  
197 input gene list to RunCCA function, and the first 4 dimensions were used as input to  
198 AlignSubspace function. The aligned projection vectors were used as input to do  
199 dimensional reduction by RunTSNE function. Perplexity was set to 40. We used the  
200 two t-SNE coordinates for adult cells to conduct KNN and re-assign foetal IN identities  
201 using the knn.cv function from R package FNN. A foetal IN was assigned the identity  
202 represented by the majority, and at least 5, of its closest 30 neighbours; in case of ties,  
203 the cell remains unassigned. t-SNE plots, and the bar plots were generated using R  
204 package ggplot2.

## 205 **Gene ontology analysis**

206 The resulting gene list, ordered by sign-adjusted P value, was the input for gene set  
207 enrichment analysis to test for enriched gene ontology (GO) terms using the  
208 clusterProfiler package version 3.4.4 with default settings. GO term analysis was  
209 performed on three categories (Biological process. Molecular function. Cellular  
210 component), and gene sets with a BH adjusted P < 0.05 were considered to be  
211 significantly enriched. The top three significant GO terms in each category were  
212 plotted by R package ggplot2.

## 213 **Animals**

214 All rats were bred in-house according to Home Office UK legislation and licenses  
215 approved by the University of Edinburgh Ethical Review Committees and Home Office.  
216 Animal husbandry was in accordance with UK Animals (Scientific Procedures) Act of  
217 1986 regulations. Rat 16p11.2 DEL rat model (*16p11.2<sup>+/-</sup>*) was generated by  
218 CRISPR/Cas9 genome editing of the Sprague Dawley line (Qiu et al., 2019). Rats



219 were maintained on the Sprague Dawley background. P21 rat tissue was fixed by  
220 transcardial perfusion with 4% paraformaldehyde in PBS, brains were then dissected  
221 and immersed in 4% paraformaldehyde in PBS overnight at 4°C.

## 222 **In Situ Hybridisation and Immunofluorescence labelling**

223 Brains were cryoprotected in 30% sucrose in PBS, embedded in OCT and sectioned  
224 at a thickness of 10µm using a cryostat (Leica, CM3050 S). Frozen sections were then  
225 mounted on SuperFrost Plus™ slides (Thermo Fisher). *Gad1* In situ hybridisation on  
226 frozen sections was performed as previously described (Wallace and Raff, 1999).  
227 NeuN Immunofluorescence was performed following in situ hybridisation as described  
228 previously (Clegg et al., 2014) with rabbit anti-NeuN (1/300, Abcam) Secondary  
229 antibodies used were donkey anti-goat Alexa Fluor 488 and donkey anti-rabbit Alexa  
230 Fluor 568 (both used 1/200 and from Life Technologies). Tissue was counterstained  
231 using DAPI (1/1000, Life Technologies).

232 Axon initial segment (AIS) labelling, was performed as previously described (Oliveira  
233 et al., 2020). Briefly, rats were perfused as described above, then post-fixed for 1 hour  
234 at room temperature with 4% paraformaldehyde in 0.1 M phosphate buffer (PB).  
235 Brains were then transferred to 0.1 M phosphate buffered saline (PBS) and 60 µm  
236 thick coronal slices containing the CA1 region of hippocampus were cut on an  
237 oscillating blade vibratome (Leica VT1000, Leica, Germany) and transferred to PBS.  
238 Briefly, sections were rinsed in PBS then transferred to a blocking solution containing  
239 10% normal goat serum, 0.3% Triton X-100 and 0.05% NaN<sub>3</sub> diluted in PBS for 1 hour.  
240 Primary antibodies raised against AnkyrinG (1:1000; 75-146, NeuroMab, USA) and  
241 somatostatin (Somatostatin-14, T-4102.0400; 1:1000, Peninsula Labs, USA) were  
242 applied in PBS containing 5% normal goat serum, 0.3% Triton X-100 and 0.05% NaN<sub>3</sub>  
243 for 24-72 hours at 4 °C. Slices were washed with PBS and then secondary antibodies  
244 applied (Goat anti-rabbit AlexaFluor 488 and Goat anti-mouse AlexaFluor 633,  
245 Invitrogen, UK, both 1:500) in PBS with 3% normal goat serum, 0.1% Triton X-100 and  
246 0.05% NaN<sub>3</sub> added, overnight at 4°C. Sections were then washed with PBS, desalted  
247 in PB, and mounted on glass slides with Vectashield® mounting medium (Vector Labs,  
248 UK). Confocal image stacks of either the *str. pyramidale* or *str. oriens/alveus* border  
249 were acquired on a Zeiss LSM800 laser scanning microscope equipped with a 63x  
250 (1.4 NA) objective lens at 1024x1024 resolution (step size of 0.25 µm). Individual AIS

251 were measured offline using ImageJ as segmented lines covering the full extent of  
252 AnkyrinG labelling observed. As in SSt INs the AIS often emerges from a proximal  
253 dendrite, they were only identified where they emerged from a clearly fluorescent  
254 labelled dendrite. A minimum of 25 AIS were measured from each rat.

255 For identification of somatostatin INs, slices were fixed following whole-cell patch-  
256 clamp recording (see below) and fixed overnight in 4% PFA in 0.1 M PB.  
257 Immunofluorescent labelling was performed according to the same protocol as above,  
258 but excluding the AnkyrinG antibody. Secondary antibodies (goat anti-rabbit  
259 AlexaFluor488, 1:500, Invitrogen, Dunfermline, UK) were applied with the added  
260 inclusion of fluorescent-conjugated streptavidin (Streptavidin AlexaFluor 633, 1:500,  
261 Invitrogen, Dunfermline, UK) to visualise recorded neurons.

262

## 263 **Imaging**

264 All fluorescence images were acquired using either a Leica AF6000 epifluorescence  
265 microscope coupled to a Leica DFC360 digital camera running Leica LAS-X software,  
266 or a Nikon Ti: E Inverted confocal microscope running Nikon NIS-Elements Confocal  
267 software.

268

## 269 **NeuN/Gad1 Cell Quantification**

270 *Gad1*<sup>+</sup> and NeuN<sup>+</sup> cells within the cortex were quantified by counting *Gad1*<sup>+</sup> (red) and  
271 NeuN<sup>+</sup> cells (green) within a 200µm wide column spanning the somatosensory cortex  
272 (indicated region, Figure 5A). *Gad1*<sup>+</sup> and NeuN<sup>+</sup> cell position was quantified by  
273 counting cells in 10 adjacent counting bins within the same 200µm wide column  
274 spanning the somatosensory cortex.

275 *Gad1*<sup>+</sup> and NeuN<sup>+</sup> cells within the hippocampus were quantified by counting cells  
276 within the *str. oriens* and *str. pyramidale* of the CA1 region (indicated region, Figure  
277 5A). To control for the varying size of the counting area *Gad1*<sup>+</sup> cell number was  
278 expressed as *Gad1*<sup>+</sup> cells per length (mm) of the CA1 region, length was measured  
279 along the centre of the *str. pyramidale*. *Gad1*<sup>+</sup> cells were classified as belonging to *str.*  
280 *pyramidale* if in contact with NeuN<sup>+</sup>; *Gad1*<sup>-</sup> pyramidal cells, all other hippocampal

281 *Gad1*<sup>+</sup> cells superficial to this layer were classified as belonging to *str. oriens*. All  
282 measurements and quantification was performed using FIJI software.

283

#### 284 ***In vitro* slice electrophysiology:**

285 Acute rat brain slices were prepared as previously described (Oliveira et al., 2021).  
286 Briefly, rats were decapitated without anaesthesia and the brain rapidly dissected into  
287 ice-cold sucrose-modified artificial cerebrospinal fluid (ACSF; in mM: 87 NaCl, 2.5 KCl,  
288 25 NaHCO<sub>3</sub>, 1.25 NaH<sub>2</sub>PO<sub>4</sub>, 25 glucose, 75 sucrose, 7 MgCl<sub>2</sub>, 0.5 CaCl<sub>2</sub>), which was  
289 saturated with carbogen (95 % O<sub>2</sub>/5 % CO<sub>2</sub>). 400 µm horizontal brain slices were cut  
290 on a vibratome (VT1200S, Leica, Germany) and transferred to sucrose-ACSF at 35°C  
291 for 30 min and then room temperature until needed.

292 For whole-cell patch-clamp recordings slices were transferred to a submerged  
293 recording chamber flowing with pre-warmed ACSF (in mM: 125 NaCl, 2.5 KCl, 25  
294 NaHCO<sub>3</sub>, 1.25 NaH<sub>2</sub>PO<sub>4</sub>, 25 glucose, 1 MgCl<sub>2</sub>, 2 CaCl<sub>2</sub>), bubbled with carbogen, and  
295 perfused a rate of 4-6 mL.min<sup>-1</sup> at 30±1 °C). Slices were viewed under infrared  
296 differential interference contrast microscopy with a digital camera (SciCamPro,  
297 Scientifica, UK) mounted on an upright microscope (SliceScope, Scientifica, UK) with  
298 40x water-immersion objective lens (1.0 N.A., Olympus, Japan). Recording pipettes  
299 were pulled from borosilicate glass capillaries (1.7 mm outer/1mm inner diameter,  
300 Harvard Apparatus, UK) on a horizontal electrode puller (P-97, Sutter Instruments, CA,  
301 USA), which when filled with a K-gluconate based internal solution (in mM 142 K-  
302 gluconate, 4 KCl, 0.5 EGTA, 10 HEPES, 2 MgCl<sub>2</sub>, 2 Na<sub>2</sub>ATP, 0.3 Na<sub>2</sub>GTP, 1  
303 Na<sub>2</sub>Phosphocreatine, 2.7 Biocytin, pH=7.4, 290-310 mOsm) which resulted in a 3-  
304 5 MΩ tip resistance. Cells were rejected if: they were more depolarised than -50 mV,  
305 had series resistance >30 MΩ, or the series resistance changed by more than 20%  
306 during the recording. Recordings were performed with a MultiClamp 700B (Molecular  
307 Devices, CA, USA) amplifier and filtered online at 10 kHz with the built-in 4-pole Bessel  
308 filter and digitized at 20 kHz (Digidata1550B, Molecular Devices, CA, USA).)

309 Cells were identified either as CA1 pyramidal cells (CA1 PCs) with having large, ovoid  
310 somata located in *str. pyramidale* and an apical dendrite entering *str. radiatum* or  
311 somatostatin INs having bipolar, horizontally oriented somata at the *str. oriens/alveus*  
312 border. All intrinsic membrane properties were measured in current-clamp. Passive

313 membrane properties, included resting membrane potential, membrane time constant,  
314 and input resistance, were measured from hyperpolarising steps (-10 pA, 500 ms  
315 duration), from resting membrane potential. Active properties were determined from a  
316 series of hyper- to depolarising current steps (-500 to +500 pA, 500 ms) from a holding  
317 potential of -70mV, maintained with a bias current injection. All AP properties were  
318 determined from the first AP elicited above rheobase. Spontaneous EPSCs were  
319 measured in voltage-clamp from a holding potential of -70mV and detected offline  
320 based on a triexponential curve fit and a threshold of 3\*SD of the baseline noise.  
321 Traces were collected in pCLAMP 9 (Molecular Devices, CA, USA) and stored on a  
322 desktop computer. Analysis of electrophysiological data was performed offline Stimfit  
323 (Guzman, Schlögl, and Schmidt-Hieber 2014), blind to both genotype. All data from  
324 somatostatin INs is shown only for those cells where clear immunofluorescent labelling  
325 was detected at the level of the soma.

#### 326 **Statistics:**

327 All rat experiments and analyses were performed blind to genotype, which were  
328 sampled in a random manner between experimental days. All data shown as mean  $\pm$   
329 standard error of the mean (SEM), with the number of cells (n) and animals (N)  
330 indicated where appropriate. All electrophysiology data are reported as cell averages.  
331 All histology data (AIS lengths and cell counts) are shown as animal averages.  
332 Minimum sample size was calculated based on our previous effect size for cellular  
333 hyperexcitability and AIS length (Booker *et al.*, 2020), assuming 80% power to  
334 determine 95% probability of rejecting the null-hypothesis. Statistical comparisons  
335 were performed using a linear mixed-effect model (or its generalised form) using the  
336 *lme4* package in R (Bates *et al.*, 2015), with genotype or cell-type as fixed effect, with  
337 slice/animal/litter included as random effects. Based on the linear mixed-effects model,  
338 p-values for statistical effects were tested using the Wald test, based on effect size  
339 and variance determined from the relevant mixed-effects model. For experiments  
340 examining the density of interneurons and principal cells, animal average densities  
341 were the principal replicate which was tested with 2-way ANOVA. Statistical  
342 significance was assumed if  $p < 0.05$ .

343

344

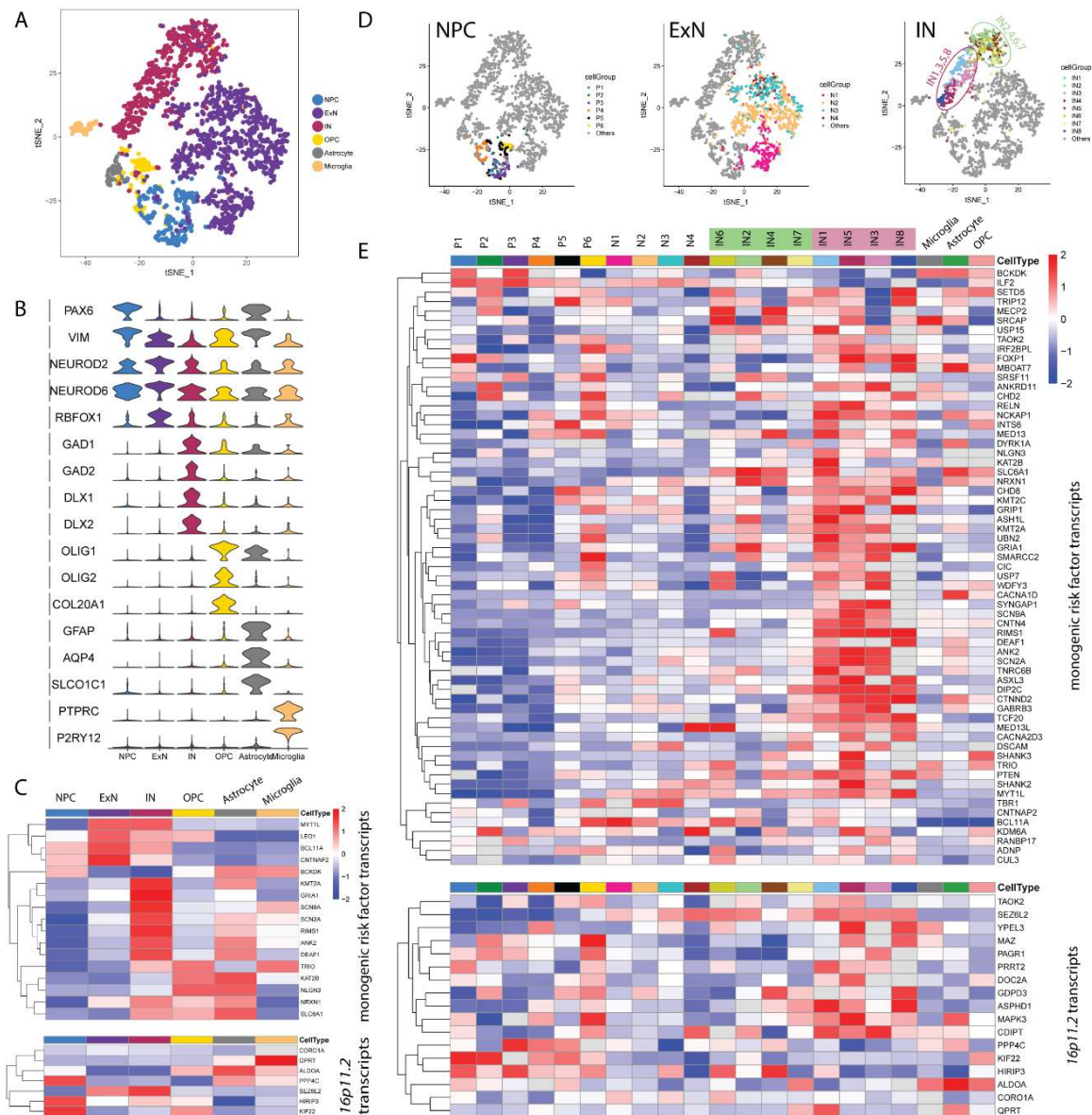
345 **RESULTS.**

346 **Differential expression of autism risk genes among foetal cortical cardinal cell**  
347 **classes**

348 A general supposition is that functional disruption of a gene will more likely affect the  
349 cells expressing high levels of it's transcript. Based on such a principle, a cell type  
350 expressing high levels of an autism associated transcript is regarded as potentially  
351 vulnerable to genetic mutation in that gene with the resulting cellular phenotype  
352 contributing to the development of autism. Accordingly, we have calculated differential  
353 expression of autism associated transcripts among cell types in foetal human cerebral  
354 cortex to identify cells potentially vulnerable to autism genetic risk factors during brain  
355 development.

356 We started with a scRNA-seq dataset comprising 2306 cells taken from human foetal  
357 pre-frontal cortex spanning gestational weeks (GW) 8 to 26 (Zhong et al., 2018). Six  
358 cardinal cell types were identified in the authors' original classification, including neural  
359 progenitor cells (NPCs), excitatory neurons (ExN), interneurons (IN), oligodendrocyte  
360 precursor cells (OPCs), astrocytes, and microglia (Fig. 1A,B and Fig. S1A,B).  
361 Differentially expressed genes (DEGs) were calculated across these six cardinal cell  
362 classes. Based on the DEGs, we find that the six cell classes showed distinct cardinal  
363 class aggregation and specific gene expression profiles associated with neural  
364 progenitor cells (NPC), excitatory neurons (ExN), inhibitory neurons (IN),  
365 oligodendrocyte precursors (OPC), astrocytes, and microglia. A list of well-known cell  
366 class markers that are included in the DEGs was used to illustrate the classification  
367 across six cardinal cell classes (Nowakowski et al., 2017, Pollen et al., 2014, Camp et  
368 al., 2015) (Fig. 1B). The markers used to identify different cardinal cell classes were:  
369 *PAX6*, *HES2* and *VIM* (NPCs); *NEUROD2*, *NEUROD6* and *RBFOX1* (ExNs); *GAD1*,  
370 *GAD2*, *DLX1* and *DLX2* (INs); *OLIG1*, *OLIG2* and *COL20A1* (OPCs); *GFAP*, *AQP4*  
371 and *SLCO1C1* (astrocytes); *PTPRC* and *P2RY12* (microglia). The expression pattern  
372 of these marker genes show that the cardinal cell classes were correctly represented  
373 in our analysis (Fig 1B).

Figure 1



374

375 **Figure 1:** (A-C) Differentially expression of autism risk factor transcripts among foetal

376 cortical cardinal cell classes. (A) *t*-SNE plot showing the cardinal cell classes identified

377 in the dataset. (B) Violin plot illustrating the expression pattern of marker genes among

378 the six cardinal cell classes. (C) Heatmap illustrating the expression pattern of

379 significantly differentially expressed autism risk factor transcripts across cardinal cell

380 classes (Wilcox test, adjust  $p < 0.05$ ,  $\log(\text{fold change}) > 0.3$ ). Top: monogenic autism

381 risk factor transcripts; Bottom: *16p11.2* transcripts. (D,E) Unsupervised clustering

382 within the cardinal classes and similarity comparison between cell clusters. (D)

383 Unsupervised clustering subdividing the cardinal classes into 21 different cell clusters.

384 OPC, astrocytes, and microglia were not further clustered. (E) Heatmap illustrating the

385 expression pattern of differentially expressed autism risk factor transcripts across 21  
386 cell clusters (Wilcoxon test, adjust  $p < 0.05$ ,  $\log(\text{fold change}) > 0.3$ ) for differentially  
387 expressed monogenic autism risk factor transcripts (top panel) and differentially  
388 expressed *16p11.2* transcripts (bottom panel).

389 Then we identified the expression pattern of autism risk factor transcripts across the  
390 cardinal cell classes and found that 17/83 high confidence and strong candidate  
391 monogenic risk factor transcripts and 7/27 *16p11.2* transcripts were significantly  
392 differentially expressed between cardinal cell classes (Fig 1C). A heatmap of  
393 expression of the monogenic autism risk factor transcripts (Fig 1C – top) and the  
394 *16p11.2* transcripts (Fig 1C – bottom) shows expression of each autism risk factor  
395 transcript (rows) in each of the six cardinal cell classes (columns). Transcript levels  
396 with expression greater than average across the cardinal classes are shown in red,  
397 while transcripts with lower than average expression are shown in blue. There was no  
398 obvious pattern to suggest that any cardinal class was particularly vulnerable to a large  
399 proportion of either monogenic autism genetic risk factors or the *16p11.2*  
400 microdeletion.

401

#### 402 **Identification of human foetal INs potentially disproportionately vulnerable to** 403 **genetic autism risk factors.**

404 The single-cell approach allows us to investigate the variability of highly expressed  
405 genes among molecularly defined cell subpopulations and identify cells within cardinal  
406 classes which may be vulnerable to genetic autism risk factors. Based on  
407 unsupervised clustering, we subdivided the cardinal classes into 21 different cell  
408 clusters (Fig. 1D): 6 for NPCs (P1-6); 4 for ExNs (N1-4); and 8 for INs (IN1-8). The  
409 non-neuronal cardinal cell classes (OPC, astrocytes, and microglia) contained small  
410 numbers of tightly clustered cells and were not further subdivided.

411 We clustered the 21 clusters according to transcriptomic similarity using  
412 MetaNeighbour analysis with ~2000 highly variable genes (Fig. S2A) and used this  
413 ordering to generate a heatmap of the 62/83 monogenic risk factor transcripts (Fig.  
414 1E, top) and 17/27 *16p11.2* transcripts genes (Fig. 1E, bottom) that were significantly  
415 differentially expressed between clusters. Violin plots of all autism risk transcripts  
416 (including those not differentially expressed between clusters) for the 83 monogenic

417 autism risk transcripts (Fig. S3A) and 27 *16p11.2* transcripts (Fig. S3B) show the  
418 expression profile in each cluster.

419 Of the differentially expressed monogenic risk factor transcripts (Fig 1E, top) a few  
420 were enriched in progenitor cells, (for example *IRF26PL*, *BCL11A*, and *CHD2*), with  
421 fewer transcripts enriched in excitatory neurons (for example *TBR1*). Other transcripts  
422 were expressed across many clusters (for example *KMT2A*, *ILF2*, *SMARCC2*,  
423 *SRSF11*, *UPF3B*, *TNRC6B*), while others showed relatively low expression across cell  
424 types (for example *GRIN2B*, *MAGEL2*, and *MET*). A striking feature of the heatmap  
425 was a preponderance of relatively high gene expression (red shading) in the IN cell-  
426 types (for example *SCN2A*, *SCN9A*, *DEAF1*, *SHANK2*, *RIMS1*, *GRIP1*, *SYNGAP1*),  
427 which was most apparent for the IN subgroups IN1,3,5,8 (purple highlight in Fig. 2E  
428 and circle in Fig. 1D) compared to IN2,4,6 7 (green highlight in Fig. 2E and circle in  
429 Fig. 1D) and other clusters.

430 We observed a similar pattern for *16p11.2* transcript expression (Fig 1E, bottom) with  
431 a preponderance of high expression in IN clusters1,3,5,8, indicating specifically  
432 enriched expression of subset of *16p11.2* transcripts (for example *SEZL6L2*, *PRRT2*,  
433 *QPRT*, and *YPEL3*) with the next highest number of enriched transcripts in progenitor  
434 clusters (for example *KIFF22* and *PPC4C*). Other transcripts are expressed both in  
435 progenitors and INs but much less in excitatory neurons (for example *MAPK3*), and  
436 others broadly across all cell clusters (for example *TMEM219*) or at very low levels in  
437 any cluster (*ASPHD1*, *C16orf54*, *C16orf92*, *SPN*, *TBX6*, *ZG16*).

438 To investigate how well the expression of autism risk factor transcripts defined the cell  
439 clusters more systematically we used MetaNeighbor analysis which reports on how  
440 similar cells are to each other based on expression of a given input gene set using  
441 AUROC scores (Crow et al., 2018). From this, we generated a pairwise comparison  
442 matrix between the 21 cell clusters (Fig. S2). Performing MetaNeighbor with the same  
443 ~2000 DEGs used to perform hierarchical clustering (Fig. S2A) we confirmed that cells  
444 in each cardinal class were generally more similar within class (red on heatmap) and  
445 less similar (blue on heatmap) between cardinal classes. Nevertheless, some neurons  
446 (N1 and N2) were quite similar to progenitors (P1-P6) likely indicating that they  
447 represented relatively immature excitatory neurons that retained some progenitor  
448 identity. Within the INs there was a clear divide between IN1,3,5,8 (red box in Fig.



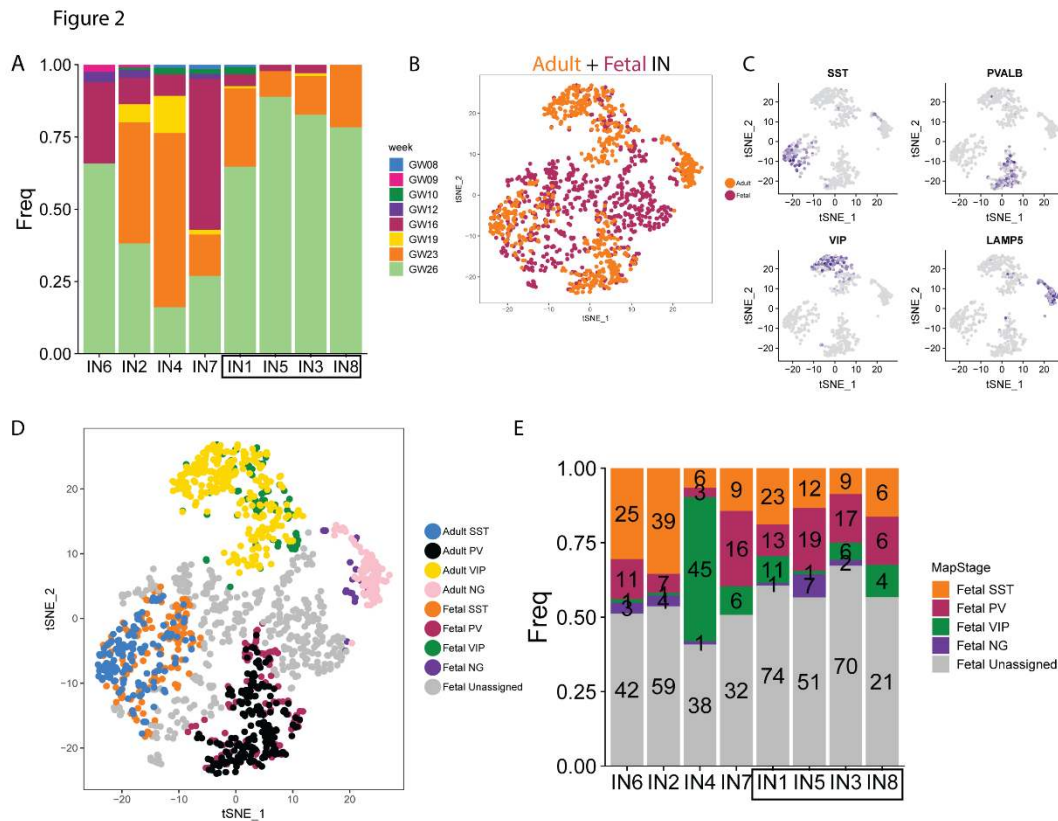
449 S2A-C) and IN2,4,6 (green box in Fig. S2A-C) cluster groups, with highest similarity  
450 within group and low similarity between groups. Next, we performed the same analysis  
451 for the 83 SFARI monogenic autism risk factor transcripts (Fig. S2B) and found that  
452 strongest similarity was retained within the progenitor group P1-P6 and the IN group  
453 IN1,3,5,8. A similar pattern emerged when we used the 27 *16p11.2* transcripts as the  
454 gene-set (Fig. S2C), although here the strongest similarity was within the progenitor  
455 group P1-6 and between IN5 and IN8. These results indicate that the immature INs  
456 can be robustly distinguished from other cells in the developing brain by their  
457 expression pattern of autism risk factor transcripts.

458 We conclude from the gene expression analysis that a subset of developing INs,  
459 IN1,3,5,8, in GW8-26 human foetal cerebral cortex express a high proportion of autism  
460 associated transcripts at higher levels than other cells. This suggests that IN1,3,5,8  
461 are vulnerable, and in some instances selectively vulnerable, to a large number of  
462 independent monogenic genetic autism risk factor and *16p11.2* microdeletion during  
463 cerebral cortex development.

464

#### 465 **Properties of human foetal INs potentially vulnerable to autism risk factors.**

466 Having identified IN1,5,3,8 as a potentially important class of INs targeted by genetic  
467 autism risk factors we next examined their developmental and transcriptional  
468 properties. We found that very few IN1,3,5,8 INs were present during the earlier stages  
469 (GW8-19) of cerebral cortex development, typically appearing from GW23 and with  
470 the vast majority of IN1,5,3,8 INs present at GW26 (Fig. 2A). On the other hand,  
471 IN2,4,6,7 clusters contained higher proportions of cells from earlier stages (Fig. 2A),  
472 suggesting that IN1,3,5,8 might represent a more mature state than the rest of IN  
473 clusters in our dataset. INs have reached the cortex in substantial numbers by GW16  
474 (Fig. S1B) indicating that IN1,3,5,8 cells correspond to a stage of the developmental  
475 trajectory after tangentially migrating INs enter the cortex (Hansen et al., 2013; Ma et  
476 al., 2013).



477

478 **Figure 2: (A)** Bar plot depicting the proportion of sample ages in each IN cluster. **(B)**  
 479 Canonical correspondence analysis (CCA) integrating the foetal and adult human  
 480 scRNA-seq data. **(C)** CCA-KNN analysis in t-SNE space provides a method to  
 481 categorise immature INs into SST, PV, VIP and Neuroglia form (NG) classes  
 482 according to their transcriptomic similarity to mature neurons from human adult cortex.  
 483 **(D)** Gradient plots showing gene expression pattern of marker genes of IN lineages in  
 484 t-SNE space. **(E)** Bar plot depicting the number and proportion of IN cell types in each  
 485 IN cluster.

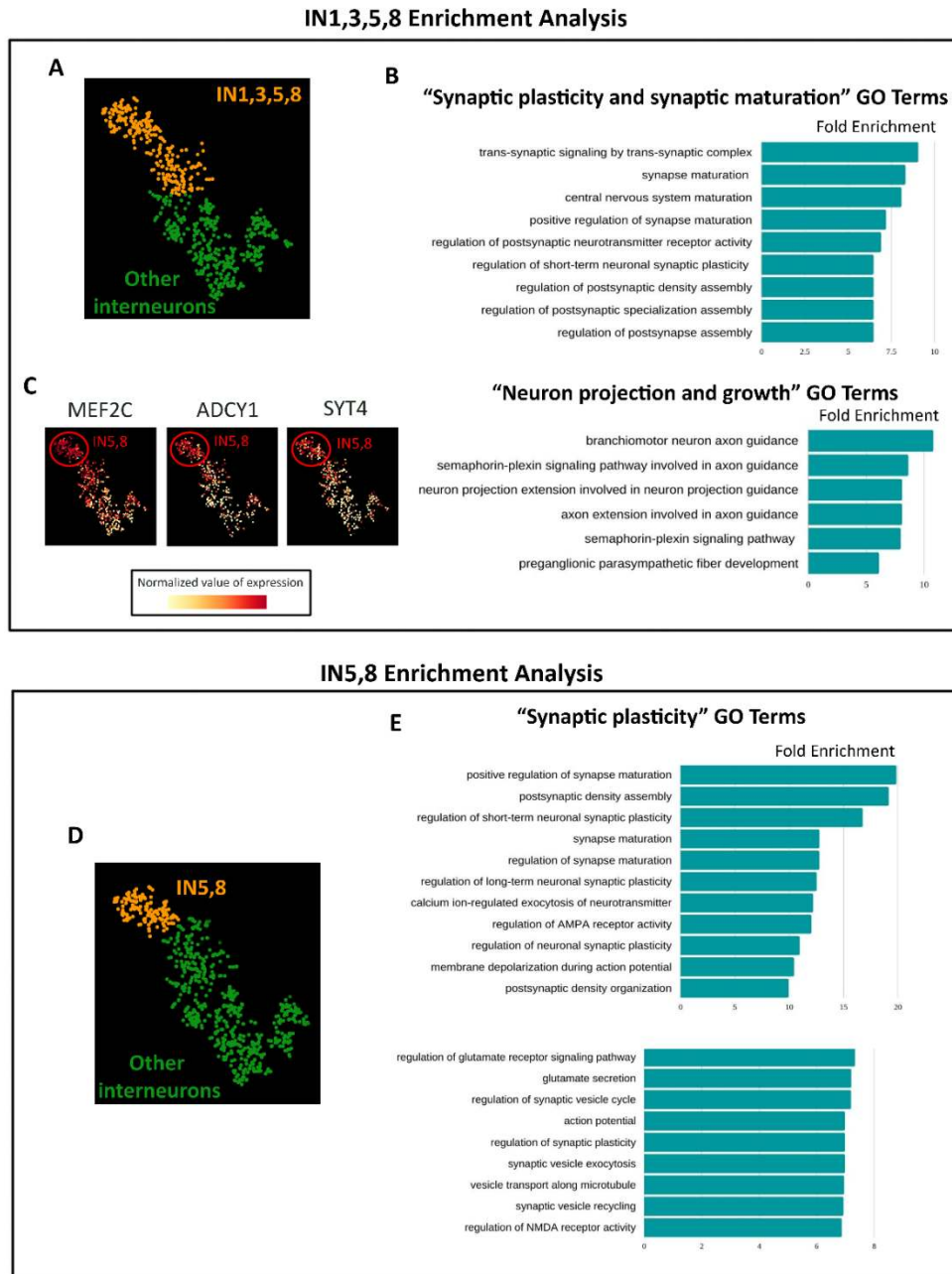
486

487 We used canonical correlation analysis (CCA-KNN) to integrate foetal (Zhong et al.,  
 488 2018) and mature (Lake et al., 2018) human IN scRNAseq datasets to identify mature  
 489 cell types corresponding to developing IN1,3,5,8 clusters. We first reduced the  
 490 dimensionality of both datasets (adult IN cells = orange; foetal IN cells = blue) onto the  
 491 same two-dimensional space using t-SNE (Fig. 2B), which allowed the identification  
 492 of 4 major cell types of adult INs based on the expression of variable genes shared  
 493 between both datasets. We then assigned identities to adult based on expression of

494 markers for PV, SST, VIP and neurogliaform cells illustrated by gradient plots of SST,  
495 *PVALB*, *VIP* and/or *LAMP5* transcripts to identify defined classes of cortical INs (Fig.  
496 2C). This then allowed us to assign foetal INs to each of these cell types based on  
497 transcriptional similarity to the mature INs (Fig. 2D). Of the IN1,3,5,8 cells classified in  
498 this manner we found that they were not homogenous, but rather consisted of PV,  
499 SST, and VIP cell types (Fig. 2E). A parsimonious interpretation is that the foetal  
500 IN1,5,3,8 are cells destined to become several categories of mature IN cell types,  
501 although this awaits further investigation as assignation of cell lineage from scRNA-  
502 seq data is ambiguous.

503 To gain further insight into the identity and developmental cell state represented by  
504 IN1,3,5,8, we first performed differential expression analysis with respect to other INs  
505 (Fig. 3A) and used the genes enriched in IN1,3,5,8 with a log fold change higher than  
506 3 (1623 genes FDR < 0.001) to test for Gene Ontology (GO, biological process)  
507 enrichment. We found that within the top 30 GO terms (ordered according to Fold  
508 Enrichment), 9 categories were related to synaptic plasticity, synaptic maturation and  
509 synaptic transmission and 6 categories were related to neuron projection and growth  
510 (Fig. 3B), with fold enrichments ranging from 6 to 10, suggesting that IN1,3,5,8 cells  
511 show earlier maturation of neurites and synapses than other INs. The Gene Ontology  
512 term “Regulation of Synaptic Plasticity” contains 192 genes, from which 54 are  
513 differentially expressed in IN1,3,5,8. A closer inspection of the expression pattern in  
514 the t-SNE space showed that many of these genes followed a general expression level  
515 gradient trend with its maximum levels in INs corresponding to IN5 and IN8 (*MEF2C*,  
516 *ADCY1*, and *SYT4* shown as examples in Fig. 3C). This suggested that the INs in the  
517 dataset must be ordered in the t-SNE space according to a gradient of synapse  
518 formation, with IN5,8 being the higher extreme of this axis. To confirm this, we  
519 performed differential expression analysis between IN5,8 IN cells versus all other INs  
520 (Fig. 3D) and found a high enrichment of synaptic plasticity-related terms but this time  
521 showing fold enrichments ranging from 7 to 20 (Fig. 3E), almost doubling the values  
522 of the previous comparison.

523



524

525 **Figure 3.** Characterisation of INs by gene ontology analysis (A-C) Gene ontology (GO)  
 526 analysis in IN1,3,5,8 (orange in A) versus other INs (green in A) reveals enrichment of  
 527 GO terms associated with (B) synaptic maturation and plasticity and axon extension  
 528 and guidance. (C) gradient plots of MEF2C, ADCY1, and SYT4 showing that these  
 529 transcripts are expressed in a gradient across INs with highest expression in IN5,8.  
 530 (D,E) Gene ontology (GO) analysis in IN5,8 (orange in D) versus other INs (green in  
 531 D) reveals enrichment of GO terms associated with (E) synaptic maturation and  
 532 plasticity.

533 Finally, to gain further insight into IN5,8 neuronal identity, we compared IN5,8 cluster  
534 versus all other neurons (including both excitatory and inhibitory, Fig. S4A).  
535 Interestingly, enriched functional terms were mainly related to synaptic plasticity,  
536 learning and social behaviour (Fig. S4B). Visual inspection of gradient plots in the t-  
537 SNE space confirmed that many of the genes linked to synaptic plasticity and  
538 maturation are selectively expressed in IN5,8 (Fig. S4C). Together this analysis  
539 suggests that IN1,3,5,8 are relatively differentiated INs elaborating processes and  
540 forming synapses.

541 This raises the possibility that by targeting the stage of the IN developmental trajectory  
542 represented by IN1,3,5,8, multiple genetic autism risk factors perturb the development  
543 of the physiological properties of foetal INs. The remaining interneurons IN2,4,6,7  
544 appear less vulnerable and may represent an earlier stage in the IN developmental  
545 trajectory or correspond to different IN lineages. Either way our analysis suggests  
546 genetic autism risk factors impact on many INs during foetal development and may  
547 affect their function into postnatal life.

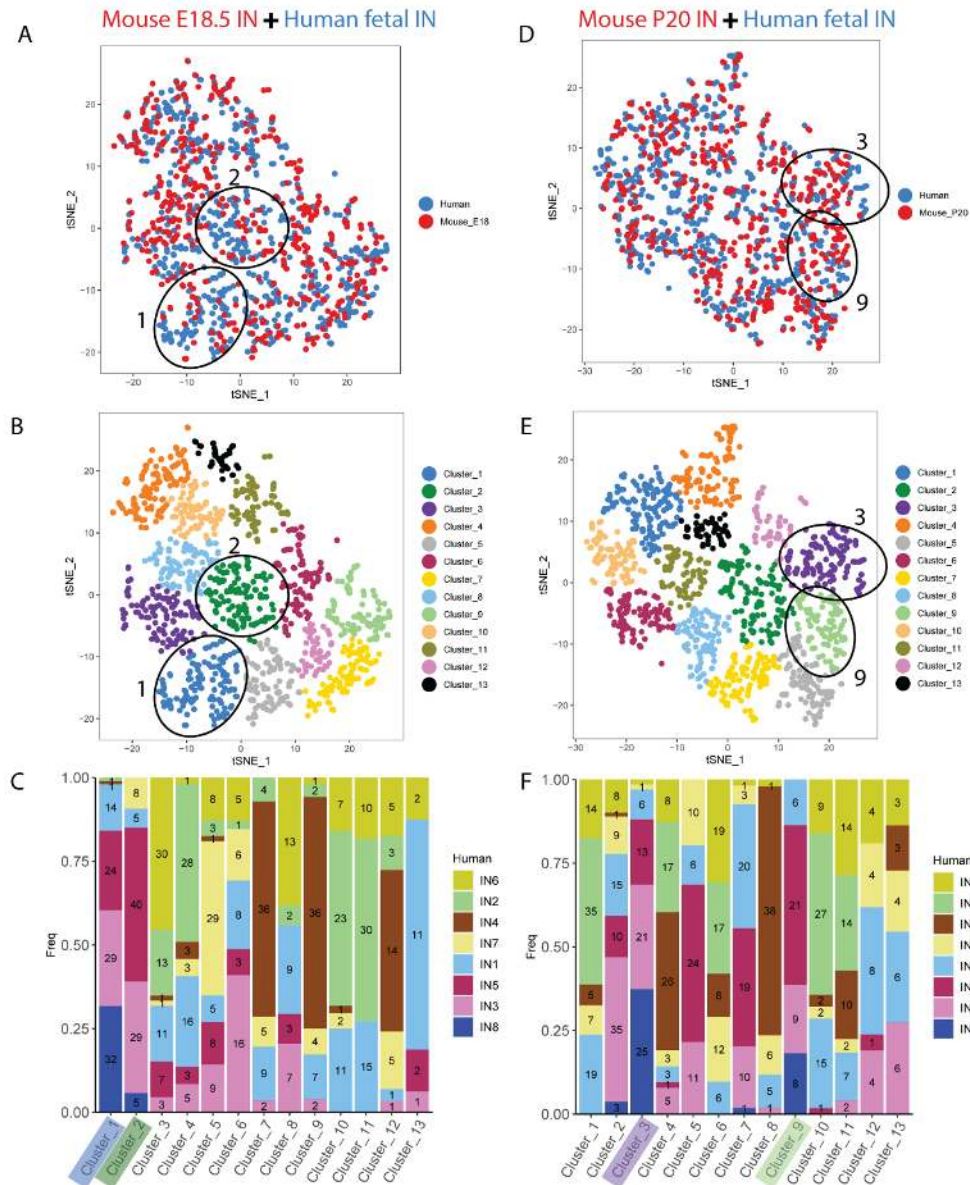
548

#### 549 **Conservation of potentially vulnerable INs between humans and rodents.**

550 These analyses of human foetal neurons suggest the testable hypothesis that a large  
551 proportion of autism related genes selectively regulate IN development in the human  
552 foetal cortex. A prediction of this hypothesis is that there will be IN phenotypes initiated  
553 during human brain development *in utero* that persist into postnatal life and predispose  
554 to autism and its comorbid conditions. Such investigation is currently not possible,  
555 however, rodent models provide a complementary means to test cellular vulnerability  
556 to autism genetic risk factors under physiological conditions. As such, we next  
557 confirmed that developing rodent brain contains INs with similar molecular properties  
558 to the potentially vulnerable human foetal INs IN1,3,5,8 identified above.

559 We identified two mouse scRNAseq data sets comprising FACS sorted cortical INs at  
560 embryonic day (E) 18.5 and postnatal (P) day 20, when INs are differentiating and  
561 forming circuits (Mayer et al., 2018). For each mouse developmental stage we used  
562 CCA-KNN to integrate the mouse and human INs into the same tSNE space (Fig. 4  
563 A,D) to allow us to identify mixed clusters of transcriptomically similar mouse and  
564 human INs (Fig. 4B,E).

Figure 4



565

566 **Figure 4:** Identifying transcriptomic correlates between developing human and mouse  
 567 INs at (A-C) E18.5 and (D-F) P20. (A,D) CCA integration of mouse (red) and human  
 568 (blue) INs in tSNE space. (B,E) JACCARD clustering into 13 mixed clusters. (C,F)  
 569 Distribution of human IN1-8 INs in each of the mixed clusters with numbers of cells  
 570 shown within each bar. The mixed clusters 1&2 for E18.5 (A-C) and 3&9 for P20 (D-  
 571 F) that are most enriched for human IN1,3,5,8 cells are indicated on each panel.

572 For each mouse developmental stage, we examined how the human IN cell types IN1-  
 573 8 were distributed between the mixed mouse+human clusters (Fig. 4C,F). This

574 analysis revealed that E18.5 clusters 1 and 2 (indicated in Fig 4A-C) and P20 clusters  
575 3 and 9 (indicated in Fig 4D-F) contained the greatest enrichment of human IN1,3,5,8  
576 cells. Critically, these clusters contained comparable numbers of mouse and human  
577 cells indicating that the developing and postnatal mouse possesses INs molecularly  
578 similar to human IN1,3,5,8 cells. These findings suggest that INs we have identified  
579 as potentially vulnerable to genetic autism risk factors are shared between humans  
580 and rodents allowing us to investigate them under physiological conditions using  
581 rodent models.

582

### 583 **Changes to IN function in the rat model of *16p11.2* microdeletion.**

584 The *16p11.2* microdeletion causes *16p11.2* transcript levels to be reduced by about  
585 50% in humans and rodent models (Tai et al., 2016) (Pucilowska et al., 2015) (Horev  
586 et al., 2011) (Blumenthal et al., 2014). As multiple *16p11.2* transcripts are normally  
587 highly enriched in developing INs (Fig. 1), we hypothesised that their simultaneous  
588 reduced expression following *16p11.2* microdeletion may synergistically impact IN  
589 development with post-natal consequences on IN phenotypes. We next set out to test  
590 this hypothesis by performing electrophysiological and anatomical interrogation of the  
591 rat *16p11.2* microdeletion model (*16p11.2*<sup>+/-</sup> rats).

592 As *16p11.2* transcripts are expressed in the ganglionic eminences where IN  
593 progenitors reside (Morson et al., 2021), we first asked if the numbers of inhibitory  
594 and/or excitatory neurons populating the cortex post-natally was different in the  
595 *16p11.2*<sup>+/-</sup> rats. To investigate this, we counted these cardinal cell classes in WT and  
596 *16p11.2*<sup>+/-</sup> rats at postnatal day (P) 21, an age by which INs have migrated into the  
597 cortex and assumed their final laminar positions forming circuits with resident  
598 excitatory neurons. We combined immunostaining for the pan-neuron-specific marker  
599 NeuN and *in situ* hybridization for the IN marker *Gad1* to identify NeuN<sup>+</sup>; *Gad1*<sup>-</sup>  
600 excitatory neurons and NeuN<sup>+</sup>; *Gad1*<sup>+</sup> INs in the cortex (Fig. 5A). Quantification within  
601 a 200µm wide column spanning the somatosensory cortex and hippocampus (shown  
602 figure 5A) shows no significant difference between WT and *16p11.2*<sup>+/-</sup> rats in total IN  
603 number ( $t_{(8)} = 0.27$ ,  $p = 0.80$  *t* test, Figure S5A) or in the proportion of the neuronal  
604 population identified as inhibitory or excitatory ( $t_{(8)} = 0.15$ ,  $p = 0.89$  *t* test, Fig. S5B). To  
605 assess whether the cortical laminar position of INs was altered in *16p11.2*<sup>+/-</sup> rats we

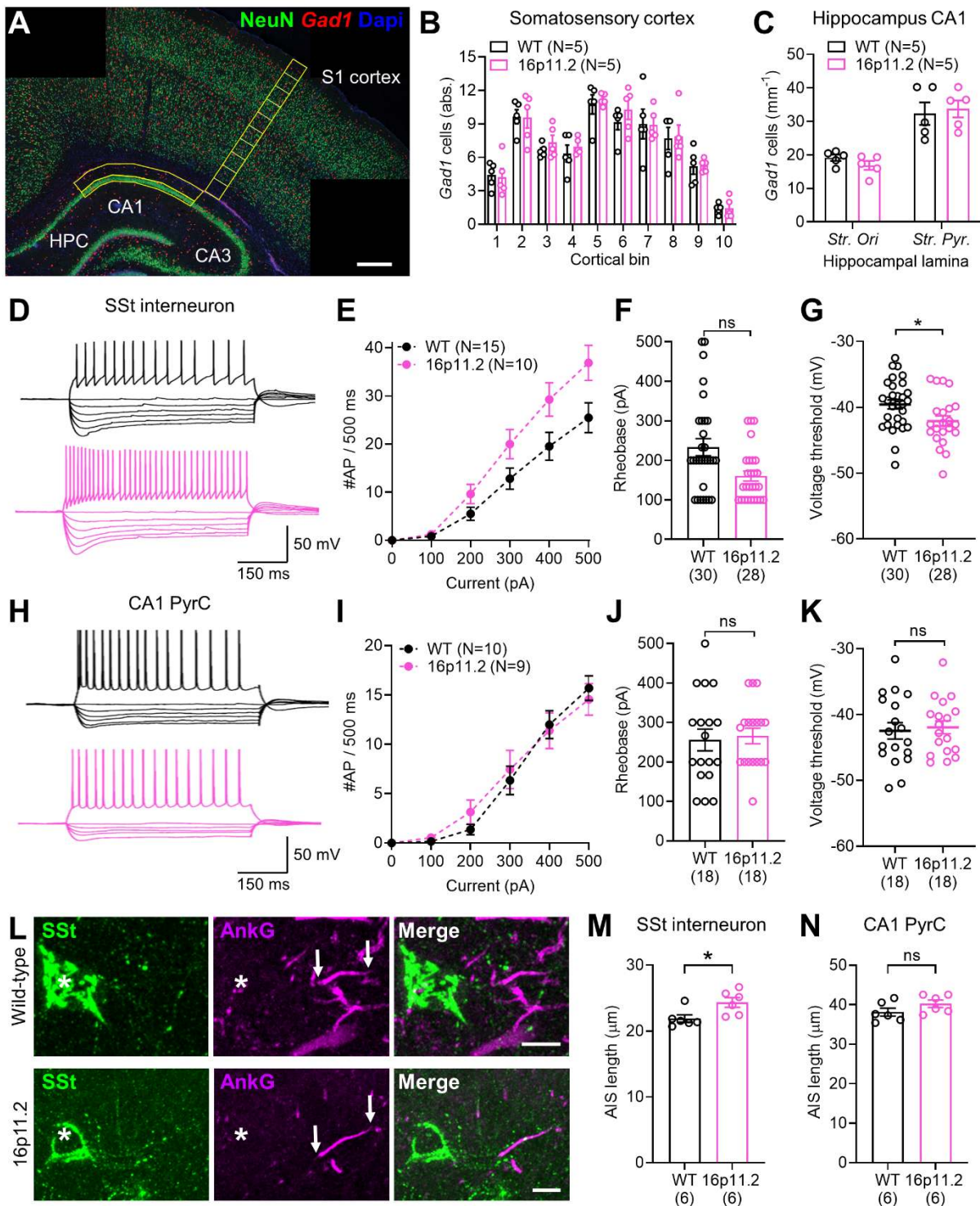
606 quantified IN and excitatory neuron number in 10 adjacent counting areas spanning  
607 the somatosensory cortex. We found no significant change in the distribution of INs  
608 across the cortex (Figure 5B), nor did we see any change in the inhibitory/excitatory  
609 proportion in any counting area (Fig. S5B). Next, we examined IN number and position  
610 in the CA1 region of the hippocampus. Total combined IN number within the *str. oriens*  
611 (SO) and *st. pyramidale* (SP) of CA1 was unchanged between WT and *16p11.2<sup>+/-</sup>* rats  
612 ( $t_{(8)} = -0.09$ ,  $p = 0.93$  *t* test, Fig. S5A). Total IN number within the SO and SP was also  
613 unchanged indicating that the position of INs within the hippocampus is unaffected in  
614 *16p11.2<sup>+/-</sup>* rats (Figure 5C). These data indicate that the *16p11.2* microdeletion does  
615 not have a major impact on number or distribution of inhibitory or excitatory neurons  
616 in the cerebral cortex or CA1 INs post-natally.

617 Our bioinformatic analysis indicated that human foetal IN1,3,5,8 cells contribute to  
618 mature somatostatin (SST) INs (Fig 2E). As such, we next asked whether the *16p11.2*  
619 microdeletion might have an effect on SSt IN development to alter their physiological  
620 properties. To test this, we performed whole-cell patch-clamp recordings from  
621 identified SSt INs and local pyramidal cells (PCs) in the CA1 region at P21.

622 We performed recordings from identified INs that expressed SSt in CA1 of the  
623 hippocampus, which also show expression of PV in parvalbumin (PV) in 50% of cells  
624 (Booker and Vida, 2018). The recorded Sst INs predominantly had horizontally  
625 oriented dendrites in *str. oriens*, which when present had an axon extending into *str.*  
626 *lacunosum-moleculare* (Booker and Vida, 2018). In the present study, we recorded  
627 from 30 WT (from 15 rats) and 28 *16p11.2<sup>+/-</sup>* (10 rats) SSt INs, which all displayed clear  
628 immunoreactivity for the SSt neuropeptide at the somata. In response to  
629 depolarising current injections (0-500 pA, 100 pA steps, Fig. 5D), SSt INs generally  
630 responded with high action potential discharge rates, which had a peak action potential  
631 discharge of  $27.4 \pm 2.5$  action potentials/500 ms (Fig. 5E). We found that SSt INs from  
632 the *16p11.2<sup>+/-</sup>* showed elevated action potential discharge, compared to WT controls  
633 ( $F_{(5, 58)} = 5.10$ ,  $P = 0.0006$  for interaction of genotype and current,  $N = 15$  WT and 10  
634 *16p11.2<sup>+/-</sup>* rats, Fig. 5E), indicating cellular hyperexcitability. Comparison of the  
635 intrinsic physiology of SSt INs revealed a general 17% reduction of rheobase current  
636 in *16p11.2<sup>+/-</sup>* compared to WT rats, albeit not significantly so ( $p = 0.1087$  LME, Fig. 5F),  
637 this was accompanied by a 6% hyperpolarisation of the voltage threshold ( $p = 0.0279$



638 LME, Fig. 5G). All other physiological parameters were similar between genotypes  
 639 (Supplementary Table S1).



640

641 **Figure 5. Selective hyperexcitability of SSt INs in *16p11.2*<sup>+/-</sup> rat hippocampus, but**  
 642 **with no change in IN number. (A) Overview micrograph of *Gad1* mRNA and NeuN**  
 643 **protein expression in the rat hippocampus and cortex at P21. *Gad1* expressing INs**

644 (red) and NeuN expressing, Gad1 negative excitatory neurons (green) can be  
645 observed in the cortex and hippocampus. Scale bars 400 $\mu$ m **(B)** Quantification of  
646 Gad1-positive IN (IN) number through the somatosensory cortex in WT (black, n=5)  
647 and 16p11.2<sup>+/-</sup> (pink, n=5) rats. Counting areas indicated yellow in A with cortical bins  
648 numbered from 1 at the ventricular edge to 10 at the pial surface. **(C)** Quantification of  
649 the combined total number of Gad1-positive neurons in the *str. oriens* (*Str. ori*) and *str.*  
650 *pyramidale* (*Str pyr.*) of the CA1 region of the hippocampus in WT (N=5) and 16p11.2<sup>+/-</sup>  
651 (N=5) rats. Counting area indicated in **A**. **(D)** Representative action potential discharge  
652 in response to hyper- to depolarising current steps in putative SSt-INs, from the *str.*  
653 *oriens* of CA1 from WT (top) and 16p11.2<sup>+/-</sup> rats (bottom). **(E)** Summary current-  
654 frequency plots from identified SSt INs from WT (N=15 rats) and 16p11.2<sup>+/-</sup> (N=10  
655 rats). **(F)** Quantification of rheobase current in identified SSt-INs from WT (n=30 cells)  
656 and 16p11.2<sup>+/-</sup> (n=28 cells) rats. **(G)** Measurement of the voltage threshold of the first  
657 action potential elicited at rheobase for the same cells in **F**. **(H-K)** the same analysis  
658 performed in CA1 pyramidal cells from WT (N=10 rats, n=18 cells) and 16p11.2<sup>+/-</sup> (N=9  
659 rats, n=18 cells). **(L)** Representative micrographs showing immunohistochemical  
660 labelling for SSt (green), the AIS marker AnkyrinG (AnkG, magenta), and their overlap  
661 (merge). The SSt soma is indicated with an asterisk (\*) and the start and end of the  
662 AIS localised to that IN indicated (arrows). Scale bar: 10  $\mu$ m. **(M)** Quantification of the  
663 AIS length of SSt INs from WT (N=6 rats, n= 162 AIS) and 16p11.2<sup>+/-</sup> (N=6 rats, n=151  
664 AIS). **(N)** Quantification of AIS lengths of putative CA1 pyramidal cells from WT (N=6  
665 rats, n= 150 AIS) and 16p11.2<sup>+/-</sup> (N=6 rats, n=155 AIS) rats. Statistics shown: ns –  
666  $p>0.05$ , \* -  $p<0.05$ , from Linear Mixed Effects modelling.

667

668 To confirm that SSt IN intrinsic excitability changes were not a result of compensation  
669 mechanism to altered synaptic input from local CA1 PCs (Booker et al., 2020), we  
670 asked whether the spontaneous excitatory postsynaptic currents (EPSC) they receive  
671 were different between genotypes. We saw no change in either the spontaneous  
672 EPSC amplitude ( $p=0.4495$ , LME) or frequency ( $p=0.2131$ , LME), implying typical  
673 circuit integration of SSt INs to the local network.

674 We confirmed that the effect on intrinsic cell excitability were restricted to SSt INs, by  
675 performing recordings from local ExNs – the CA1 PCs. CA1 PCs were identified on

676 the basis of having a somata located in *str. pyramidale*, with a single large-calibre  
677 apical dendrite entering *str. radiatum* as observed under IR-DIC. We obtained  
678 recordings from 18 putative CA1 PCs per group from 10 WT and 9 *16p11.2*<sup>+/-</sup> rats. In  
679 response to depolarising current injections (0-500 pA, 100 pA steps, Fig. 5H), we  
680 observed no change in the number of action potentials generated by the recorded CA1  
681 PCs in the *16p11.2*<sup>+/-</sup> rats compared to WT ( $F_{(5, 85)}=0.9185$ ,  $P=0.4731$ , 2-way ANOVA  
682 for current/genotype interaction, Fig. 5I). CA1 PCs typically had lower peak action  
683 potential discharge rates than for SSt INs (WT:  $p=3.29 \times 10^{-5}$ , *16p11.2*<sup>+/-</sup>:  $p=1.63 \times 10^{-6}$ ;  
684 LME). Consistent with this lack of altered action potential discharge, we found no  
685 change in CA1 PC rheobase current ( $p=0.7098$ , LME, Fig. 5J), action potential  
686 threshold ( $p=0.4116$ , LME, Fig. 5K), or any other parameter tested (Supplementary  
687 Table S1). These data strongly suggest that excitatory CA1 PCs are physiologically  
688 typical in the *16p11.2* rat model of ASD.

689 We have recently shown that changes to cell excitability effected the voltage threshold  
690 and action potential discharge in genetic models of intellectual disability can result  
691 from changes to the structure of the axon initial segment (AIS) (Booker et al., 2020).  
692 To determine if the changes in SSt IN excitability arise from changes to AIS structure  
693 we next performed immunolabelling of perfusion fixed tissue from the hippocampus of  
694 WT (N=5) and *16p11.2*<sup>+/-</sup> (N=5) rats. Immunofluorescent double labelling with  
695 AnkyrinG reliably labelled the AIS of all neurons in the CA1 region, which could be  
696 identified emerging from the soma, or more often the proximal dendrites of  
697 immunolabelled SSt INs (Fig. 5L). Comparison of AIS lengths on SSt INs revealed an  
698 11% longer AIS in *16p11.2*<sup>+/-</sup> rats compared to WT ( $p=0.0064$ , LME, Fig. 5M). There  
699 was no change in the lengths of putative CA1 PC AISs between genotypes ( $p=0.0962$ ,  
700 LME, Fig. 5N).

701 Together, consistent with the hypothesis that the *16p11.2* microdeletion selectively  
702 targets INs, these data show a preferential increase of SSt IN excitability in the  
703 *16p11.2* rat autism model, with no changes observed in the local excitatory principal  
704 cells. This increased cellular excitability coincided with selective alteration to the length  
705 of the AIS, corresponding to changes in voltage threshold. Together, these changes  
706 could potentially lead to an aberrant network activity and gating of information flow  
707 through hippocampal circuits.

## 708 **DISCUSSION.**

709 This study reveals that molecularly defined classes of INs in the foetal human cerebral  
710 cortex display enriched expression of multiple gene transcripts associated with autism.  
711 This result is striking, suggesting the testable hypothesis that some INs are  
712 disproportionately vulnerable to autism genetic risk factors. Within INs as a whole the  
713 most autism associated transcripts are enriched in a subset we described as  
714 'IN1,3,5,8' suggesting that these cells may represent a convergent cellular target  
715 underpinning genetic predisposition of the developing brain to autism and its co-  
716 occurring conditions during post-natal life. This poses the question of what is the  
717 identity of these cells? Our data-set was acquired from dissected human foetal cortex,  
718 which includes INs that are migrating tangentially through and in the cerebral cortex,  
719 but not INs undergoing neurogenesis or early migration in the ganglionic eminences  
720 (Hansen et al., 2013; Ma et al., 2013). We examined human foetal cortical cells  
721 spanning the interval GW8-26 and found IN1,3,5,8 cells are not present in the cerebral  
722 cortex before GW23 and then increase in numbers to GW26. As many INs have  
723 migrated into the cortex well before GW23 this suggests that IN1,3,5,8 represent a  
724 relatively differentiated stage on the IN developmental trajectory. This is consistent  
725 with the enrichment of GO terms relating to synapse maturation and neurite formation  
726 in these cells. Transcriptomic similarity between foetal IN1,3,5,8 and adult PV, SST,  
727 and VIP INs suggests these cells are destined to form a variety of IN cell types and  
728 that changes in their developmental trajectory caused by autism causing mutations  
729 may have far reaching consequences for the formation on inhibitory circuitry in the  
730 post-natal brain.

731 Although the most striking enrichment of autism associated transcripts was observed  
732 in INs we also saw enrichment of some transcripts in other cardinal cell classes.  
733 Progenitor cells had a much smaller number of enriched autism associated transcripts  
734 than INs and most of these (eg *ADNF*, *ZNF462*, *PHIP*, *HNRNPU*, *RPS6KA3* for  
735 monogenic and *PAGR1*, *HIRIP3*, *KIF22*, and *PP4C* for *16p11.2* transcripts). This  
736 suggests that progenitor cells in the cerebral cortex may also be vulnerable to a subset  
737 of autism causing mutations. Progenitors in the developing neocortex are destined to  
738 differentiate into excitatory pyramidal neurons and non-neuronal cell-types (eg  
739 astrocytes) suggesting that mutations in these progenitor enriched genes may  
740 dysregulate their production or function. This study also prompts future investigation

741 into the expression of autism associated transcripts in IN progenitors located in the  
742 ganglionic eminences and the consequence of mutation for IN neurogenesis in  
743 humans although our findings in the rat *16p11.2* microdeletion rat model suggest that  
744 gross IN output is not affected in this context in rodents.

745 We found that large numbers of monogenic autism risk factor transcripts are highly  
746 expressed in IN1,3,5,8 INs, suggesting that their mutation may contribute to the  
747 aetiology of autism via alterations to IN development. This hypothesis remains to be  
748 tested for the majority of genes. However, for *ARID1B*, *DYRK1A*, *MECP2*, and  
749 *CNTNAP2* there is already evidence that monogenic mutation causes abnormal  
750 numbers or physiological properties of INs in rodent models (Gao et al., 2018; Jung et  
751 al., 2017; Penagarikano et al., 2011; Souchet et al., 2019; Tomassy et al., 2014; Vogt  
752 et al., 2018). We also found *KCTD13*, *MAPK3*, and *MVP* transcripts expressed from  
753 the *16p11.2* locus are enriched in IN1,3,5,8. *KCTD13* modulates synaptic transmission  
754 by suppressing RHOA signalling via interaction with the ubiquitin ligase *CUL3*, itself  
755 an autism risk factor (Escamilla et al., 2017; Willsey et al., 2013). *CUL3* is co-  
756 expressed with *KCTD13* in IN1,3,5,8 cells suggesting a molecular mechanism for the  
757 *16p11.2* microdeletion to impact on cellular and synaptic function via perturbed RHOA  
758 signalling. Interestingly, the inhibition of RHOA pathway has been proposed as a  
759 treatment to restore cognition in *16p11.2* mouse models (Martin Lorenzo et al., 2021).  
760 *MAPK3* and *MVP* are both implicated in ERK signalling which impacts diverse cellular  
761 processes including cell proliferation, migration, and synaptic function. Indeed, a  
762 mouse model of *16p11.2* microdeletion shows elevated ERK signalling leading to  
763 perturbed cortical development and autism-like phenotypes (Pucilowska et al., 2018;  
764 Pucilowska et al., 2015), although the involvement of INs was not tested.

765 Our analysis of the *16p11.2* microdeletion rat indicates that neither ExN or IN number  
766 and location were altered in the cerebral cortex or hippocampal region CA1, so it  
767 seems unlikely that a numerical excitation/inhibition imbalance is present in the  
768 *16p11.2*<sup>+/-</sup> rat model. However, whole-cell patch-clamp recordings in CA1 revealed  
769 intrinsic hyperexcitability of SSt INs, coincident with increases AIS length. No effect  
770 was observed in CA1 excitatory neurons. This suggests a mechanism by which the  
771 *16p11.2* microdeletion perturbs the E/I balance by selectively altering the intrinsic  
772 excitability of INs. Although IN hyperexcitability may lead to greater inhibition within  
773 cortical circuits and tilt the E/I balance towards inhibition, the complexity of such

774 circuits interaction makes prediction of the consequences to gross activity difficult.  
775 However, SSt INs themselves possess both direct inhibitory and disinhibitory  
776 mechanisms within the prototypical CA1 circuit, leading to alterations to synaptic  
777 plasticity when measured at the circuit level (Leao et al., 2012). As such, the outcome  
778 of greater SSt IN activity may directly lead to altered cognition observed in ASC/ID.  
779 Furthermore, a shift in the E/I balance has been identified in the somatosensory cortex  
780 of ASC mouse models (including *16p11.2*<sup>+/-</sup> mice), attributed to homeostatic regulation  
781 of IN function (Antoine et al., 2019). Our combined bioinformatic and physiological  
782 approach diverges from this view, suggesting that SSt INs in *16p11.2* microdeletion  
783 are genetically cued to perturbation from early in their developmental trajectory. A  
784 deeper understanding of the functional consequences of SSt hyperexcitability on the  
785 E/I balance in cortical circuits and their homeostasis requires further investigation.

786 To conclude, our bioinformatic analysis of developing human foetal cerebral cortex  
787 single cell transcriptomes suggests that developing INs are disproportionately  
788 vulnerable to genetic autism risk factors, which is supported by physiological  
789 correlates in a *16p11.2* microdeletion rat model. This study paves the way for more in  
790 depth investigations of how polygenic and monogenic autism risk factors impact on IN  
791 development and function.

792

## 793 REFERENCES

794 Antoine, M.W., Langberg, T., Schnepel, P., Feldman, D.E., 2019. Increased  
795 Excitation-Inhibition Ratio Stabilizes Synapse and Circuit Excitability in Four Autism  
796 Mouse Models. *Neuron* 101, 648-661 e644.

797 Blumenthal, I., Ragavendran, A., Erdin, S., Klei, L., Sugathan, A., Guide, J.R.,  
798 Manavalan, P., Zhou, J.Q., Wheeler, V.C., Levin, J.Z., Ernst, C., Roeder, K., Devlin,  
799 B., Gusella, J.F., Talkowski, M.E., 2014. Transcriptional consequences of *16p11.2*  
800 deletion and duplication in mouse cortex and multiplex autism families. *Am J Hum*  
801 *Genet* 94, 870-883.

802 Booker, S.A., Simoes de Oliveira, L., Anstey, N.J., Kozic, Z., Dando, O.R., Jackson,  
803 A.D., Baxter, P.S., Isom, L.L., Sherman, D.L., Hardingham, G.E., Brophy, P.J.,  
804 Wyllie, D.J.A., Kind, P.C., 2020. Input-Output Relationship of CA1 Pyramidal

805 Neurons Reveals Intact Homeostatic Mechanisms in a Mouse Model of Fragile X  
806 Syndrome. *Cell Rep* 32, 107988.

807 Booker, S.A., Vida, I., 2018. Morphological diversity and connectivity of hippocampal  
808 interneurons. *Cell Tissue Res* 373, 619-641.

809 Bozzi, Y., Provenzano, G., Casarosa, S., 2018. Neurobiological bases of autism-  
810 epilepsy comorbidity: a focus on excitation/inhibition imbalance. *Eur J Neurosci* 47,  
811 534-548.

812 Crow, M., Paul, A., Ballouz, S., Huang, Z.J., Gillis, J., 2018. Characterizing the  
813 replicability of cell types defined by single cell RNA-sequencing data using  
814 MetaNeighbor. *Nat Commun* 9, 884.

815 Escamilla, C.O., Filonova, I., Walker, A.K., Xuan, Z.X., Holehonnur, R., Espinosa, F.,  
816 Liu, S., Thyme, S.B., Lopez-Garcia, I.A., Mendoza, D.B., Usui, N., Ellegood, J.,  
817 Eisch, A.J., Konopka, G., Lerch, J.P., Schier, A.F., Speed, H.E., Powell, C.M., 2017.  
818 *Kctd13* deletion reduces synaptic transmission via increased RhoA. *Nature* 551, 227-  
819 231.

820 Gao, R., Piguel, N.H., Melendez-Zaidi, A.E., Martin-de-Saavedra, M.D., Yoon, S.,  
821 Forrest, M.P., Myczek, K., Zhang, G., Russell, T.A., Csernansky, J.G., Surmeier,  
822 D.J., Penzes, P., 2018. *CNTNAP2* stabilizes interneuron dendritic arbors through  
823 *CASK*. *Mol Psychiatry* 23, 1832-1850.

824 Hansen, D.V., Lui, J.H., Flandin, P., Yoshikawa, K., Rubenstein, J.L., Alvarez-Buylla,  
825 A., Kriegstein, A.R., 2013. Non-epithelial stem cells and cortical interneuron  
826 production in the human ganglionic eminences. *Nat Neurosci* 16, 1576-1587.

827 Horev, G., Ellegood, J., Lerch, J.P., Son, Y.E., Muthuswamy, L., Vogel, H., Krieger,  
828 A.M., Buja, A., Henkelman, R.M., Wigler, M., Mills, A.A., 2011. Dosage-dependent  
829 phenotypes in models of 16p11.2 lesions found in autism. *Proc Natl Acad Sci U S A*  
830 108, 17076-17081.

831 Jung, E.M., Moffat, J.J., Liu, J., Dravid, S.M., Gurumurthy, C.B., Kim, W.Y., 2017.  
832 *Arid1b* haploinsufficiency disrupts cortical interneuron development and mouse  
833 behavior. *Nat Neurosci* 20, 1694-1707.

834 Lake, B.B., Chen, S., Sos, B.C., Fan, J., Kaeser, G.E., Yung, Y.C., Duong, T.E.,  
835 Gao, D., Chun, J., Kharchenko, P.V., Zhang, K., 2018. Integrative single-cell analysis  
836 of transcriptional and epigenetic states in the human adult brain. *Nat Biotechnol* 36,  
837 70-80.

838 Leao, R.N., Mikulovic, S., Leao, K.E., Munguba, H., Gezelius, H., Enjin, A., Patra, K.,  
839 Eriksson, A., Loew, L.M., Tort, A.B., Kullander, K., 2012. OLM interneurons  
840 differentially modulate CA3 and entorhinal inputs to hippocampal CA1 neurons. *Nat*  
841 *Neurosci* 15, 1524-1530.

842 Ma, T., Wang, C., Wang, L., Zhou, X., Tian, M., Zhang, Q., Zhang, Y., Li, J., Liu, Z.,  
843 Cai, Y., Liu, F., You, Y., Chen, C., Campbell, K., Song, H., Ma, L., Rubenstein, J.L.,  
844 Yang, Z., 2013. Subcortical origins of human and monkey neocortical interneurons.  
845 *Nat Neurosci* 16, 1588-1597.

846 Martin Lorenzo, S., Nalesso, V., Chevalier, C., Birling, M.C., Herault, Y., 2021.  
847 Targeting the RHOA pathway improves learning and memory in adult *Kctd13* and  
848 16p11.2 deletion mouse models. *Mol Autism* 12, 1.

849 Mayer, C., Hafemeister, C., Bandler, R.C., Machold, R., Batista Brito, R., Jaglin, X.,  
850 Allaway, K., Butler, A., Fishell, G., Satija, R., 2018. Developmental diversification of  
851 cortical inhibitory interneurons. *Nature* 555, 457-462.

852 Morson, S., Yang, Y., Price, D.J., Pratt, T., 2021. Expression of Genes in the  
853 16p11.2 Locus during Development of the Human Fetal Cerebral Cortex. *Cereb*  
854 *Cortex*.

855 Nelson, S.B., Valakh, V., 2015. Excitatory/Inhibitory Balance and Circuit  
856 Homeostasis in Autism Spectrum Disorders. *Neuron* 87, 684-698.

857 Oliveira, L.S., Sumera, A., Booker, S.A., 2021. Repeated whole-cell patch-clamp  
858 recording from CA1 pyramidal cells in rodent hippocampal slices followed by axon  
859 initial segment labeling. *STAR Protoc* 2, 100336.

860 Packer, A., 2016. Neocortical neurogenesis and the etiology of autism spectrum  
861 disorder. *Neurosci Biobehav Rev* 64, 185-195.

862 Penagarikano, O., Abrahams, B.S., Herman, E.I., Winden, K.D., Gdalyahu, A., Dong,  
863 H., Sonnenblick, L.I., Gruver, R., Almajano, J., Bragin, A., Golshani, P.,  
864 Trachtenberg, J.T., Peles, E., Geschwind, D.H., 2011. Absence of *CNTNAP2* leads  
865 to epilepsy, neuronal migration abnormalities, and core autism-related deficits. *Cell*  
866 147, 235-246.

867 Pucilowska, J., Vithayathil, J., Pagani, M., Kelly, C., Karlo, J.C., Robol, C., Morella,  
868 I., Gozzi, A., Brambilla, R., Landreth, G.E., 2018. Pharmacological Inhibition of ERK  
869 Signaling Rescues Pathophysiology and Behavioral Phenotype Associated with  
870 16p11.2 Chromosomal Deletion in Mice. *J Neurosci* 38, 6640-6652.



871 Pucilowska, J., Vithayathil, J., Tavares, E.J., Kelly, C., Karlo, J.C., Landreth, G.E.,  
872 2015. The 16p11.2 deletion mouse model of autism exhibits altered cortical  
873 progenitor proliferation and brain cytoarchitecture linked to the ERK MAPK pathway.  
874 *J Neurosci* 35, 3190-3200.

875 Puts, N.A.J., Wodka, E.L., Harris, A.D., Crocetti, D., Tommerdahl, M., Mostofsky,  
876 S.H., Edden, R.A.E., 2017. Reduced GABA and altered somatosensory function in  
877 children with autism spectrum disorder. *Autism Res* 10, 608-619.

878 Qiu, Y., Arbogast, T., Lorenzo, S.M., Li, H., Tang, S.C., Richardson, E., Hong, O.,  
879 Cho, S., Shanta, O., Pang, T., Corsello, C., Deutsch, C.K., Chevalier, C., Davis,  
880 E.E., Iakoucheva, L.M., Hérault, Y., Katsanis, N., Messer, K., Sebat, J., 2019.  
881 Oligogenic Effects of 16p11.2 Copy-Number Variation on Craniofacial Development.  
882 *Cell Rep* 28, 3320-3328 e3324.

883 Rapanelli, M., Frick, L.R., Pittenger, C., 2017. The Role of Interneurons in Autism  
884 and Tourette Syndrome. *Trends Neurosci* 40, 397-407.

885 Robertson, C.E., Ratai, E.M., Kanwisher, N., 2016. Reduced GABAergic Action in  
886 the Autistic Brain. *Curr Biol* 26, 80-85.

887 Souchet, B., Duchon, A., Gu, Y., Dairou, J., Chevalier, C., Daubigny, F., Nalesso,  
888 V., Creau, N., Yu, Y., Janel, N., Hérault, Y., Delabar, J.M., 2019. Prenatal treatment  
889 with EGCG enriched green tea extract rescues GAD67 related developmental and  
890 cognitive defects in Down syndrome mouse models. *Sci Rep* 9, 3914.

891 Tai, D.J., Ragavendran, A., Manavalan, P., Stortchevoi, A., Seabra, C.M., Erdin, S.,  
892 Collins, R.L., Blumenthal, I., Chen, X., Shen, Y., Sahin, M., Zhang, C., Lee, C.,  
893 Gusella, J.F., Talkowski, M.E., 2016. Engineering microdeletions and  
894 microduplications by targeting segmental duplications with CRISPR. *Nat Neurosci*  
895 19, 517-522.

896 Tomassy, G.S., Morello, N., Calcagno, E., Giustetto, M., 2014. Developmental  
897 abnormalities of cortical interneurons precede symptoms onset in a mouse model of  
898 Rett syndrome. *J Neurochem* 131, 115-127.

899 Vogt, D., Cho, K.K.A., Shelton, S.M., Paul, A., Huang, Z.J., Sohal, V.S., Rubenstein,  
900 J.L.R., 2018. Mouse *Cntnap2* and Human *CNTNAP2* ASD Alleles Cell Autonomously  
901 Regulate PV+ Cortical Interneurons. *Cereb Cortex* 28, 3868-3879.

902 Willsey, A.J., Sanders, S.J., Li, M., Dong, S., Tebbenkamp, A.T., Muhle, R.A., Reilly,  
903 S.K., Lin, L., Fertuzinhos, S., Miller, J.A., Murtha, M.T., Bichsel, C., Niu, W., Cotney,  
904 J., Ercan-Sencicek, A.G., Gockley, J., Gupta, A.R., Han, W., He, X., Hoffman, E.J.,

905 Klei, L., Lei, J., Liu, W., Liu, L., Lu, C., Xu, X., Zhu, Y., Mane, S.M., Lein, E.S., Wei,  
906 L., Noonan, J.P., Roeder, K., Devlin, B., Sestan, N., State, M.W., 2013.  
907 Coexpression networks implicate human midfetal deep cortical projection neurons in  
908 the pathogenesis of autism. *Cell* 155, 997-1007.  
909 Zhong, S., Zhang, S., Fan, X., Wu, Q., Yan, L., Dong, J., Zhang, H., Li, L., Sun, L.,  
910 Pan, N., Xu, X., Tang, F., Zhang, J., Qiao, J., Wang, X., 2018. A single-cell RNA-seq  
911 survey of the developmental landscape of the human prefrontal cortex. *Nature* 555,  
912 524-528.

913

914

915

916

917

918

919

920

921

922

923

924

925

926

927

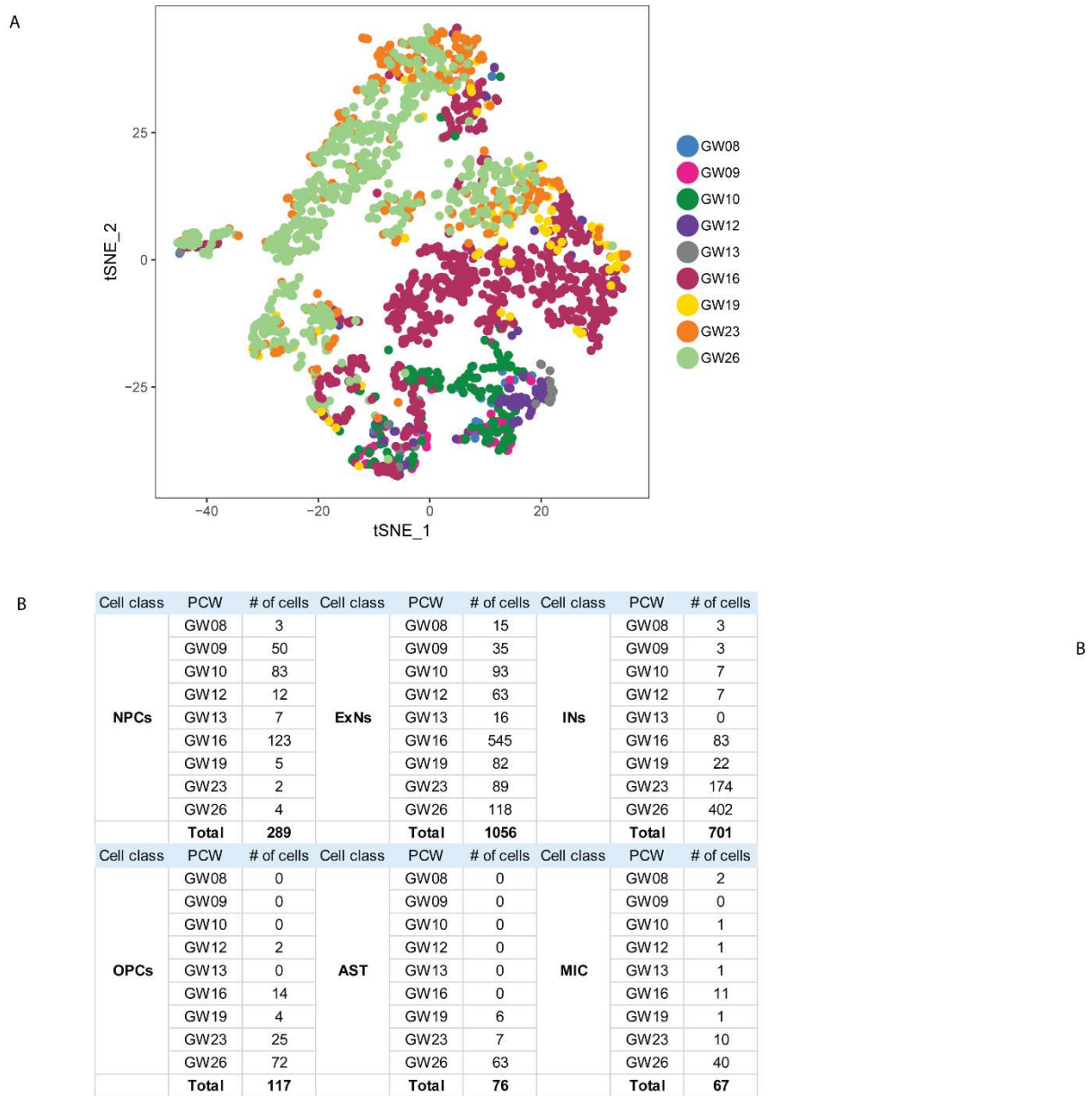
928

929

930

931 **SUPPLEMENTARY FIGURES**

Figure S1



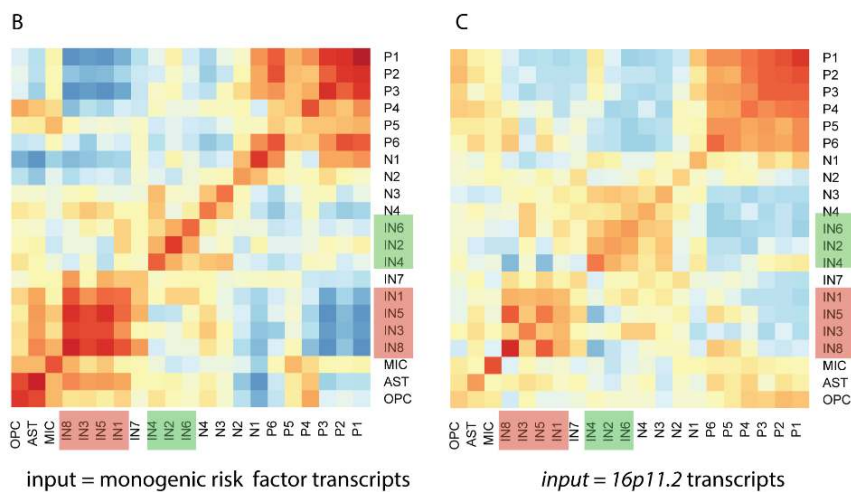
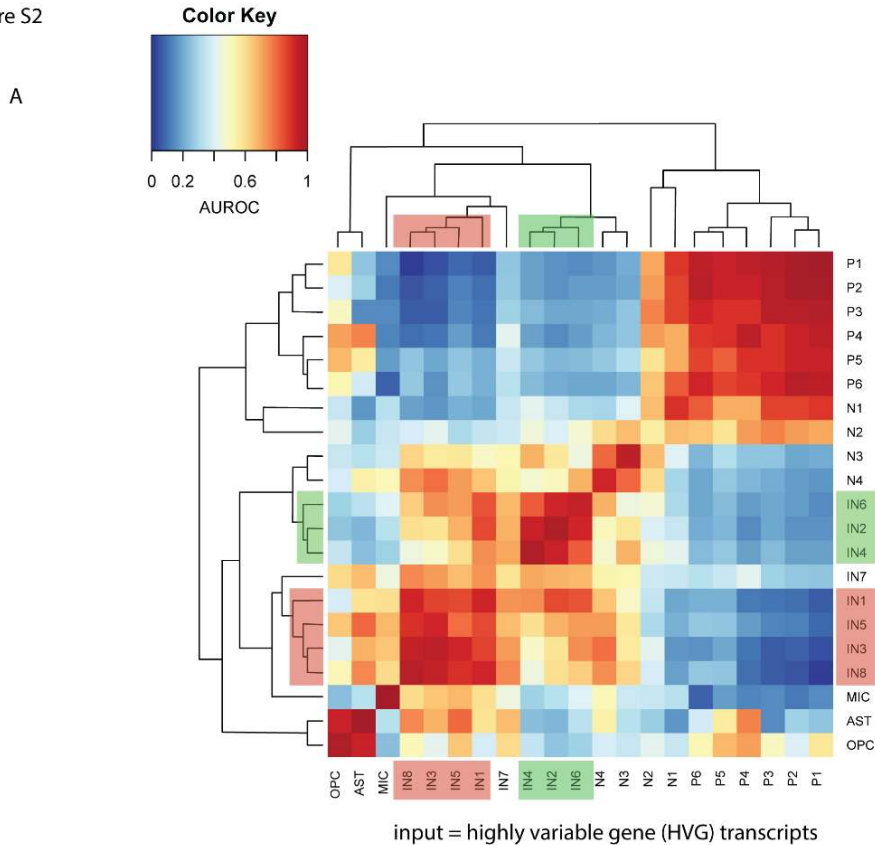
932

933 **Figure S1 (A) t-SNE plot showing the distribution of foetal stages (B) table showing**

934 **numbers of cells of each cardinal class at each foetal stage.**

935

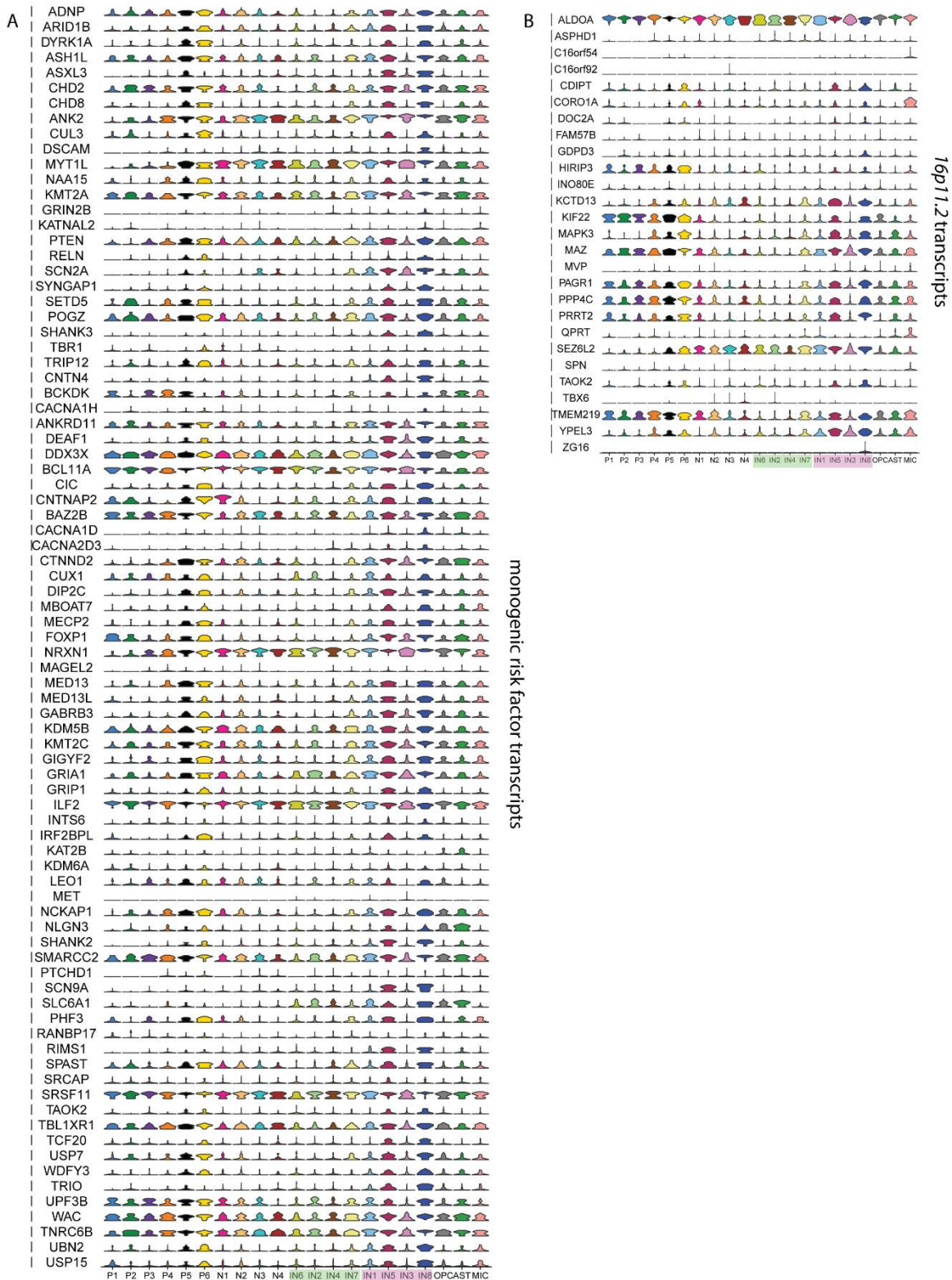
Figure S2



936

937 **Figure S2** Pairwise comparison of the cluster similarity calculated by MetaNeighbor  
 938 between the 21 cell clusters. AUROC scores represented as a heatmap where high  
 939 similarity between clusters is coloured red and low similarity blue. Three plots are  
 940 shown using different input gene sets **(A)** ~2000 highly variable gene transcripts  
 941 between clusters. **(B)** the 83 high confidence and strong candidate (SFARI lists 1 and  
 942 2) monogenic autism risk factor transcripts. **(C)** the 27 16p11.2 transcripts.

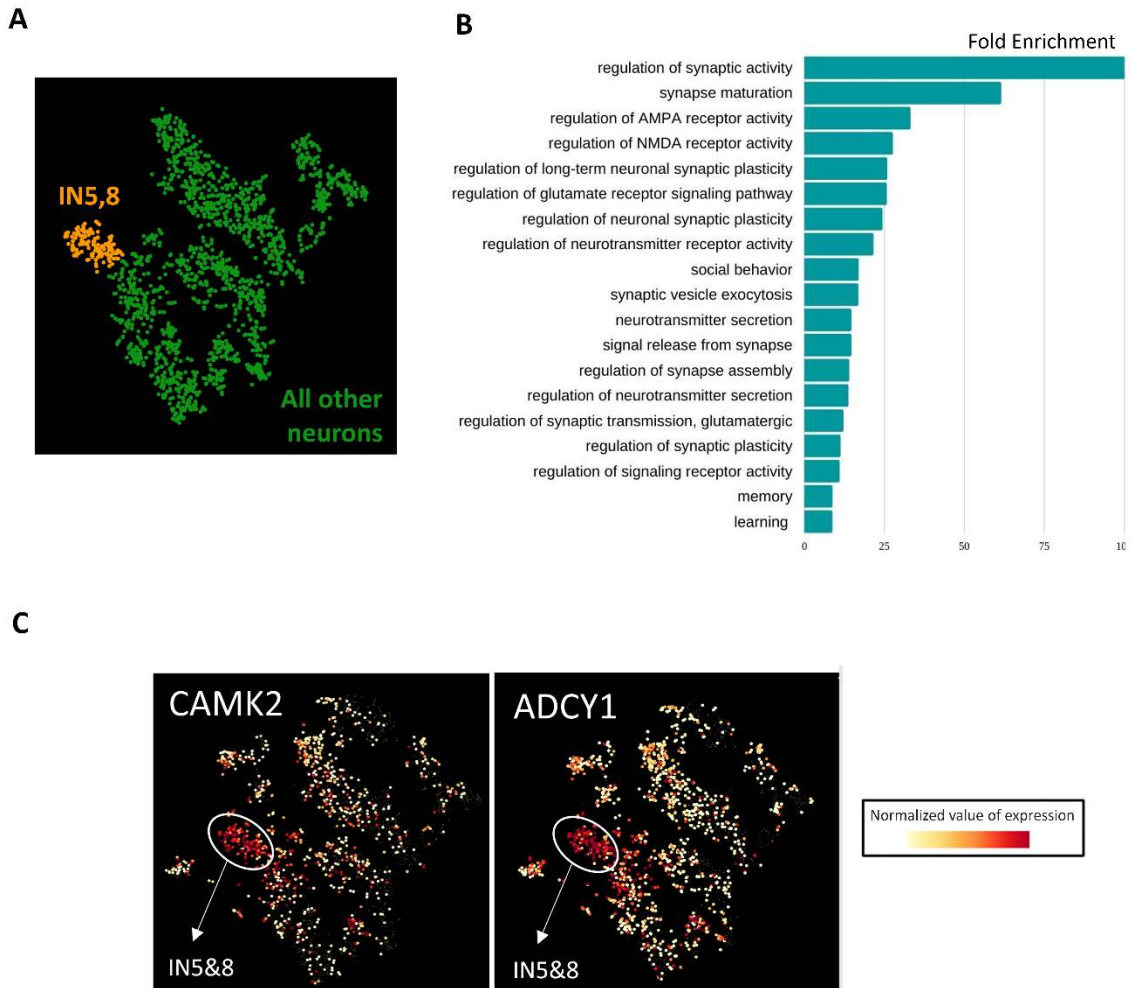
Figure S3



943

944 **Figure S3** Violin plots showing transcript levels in the 21 different clusters for **(A)** the  
 945 **83** high confidence and strong candidate (SFARI lists 1 and 2) monogenic autism risk  
 946 **transcripts** and **(B)** the 27 *16p11.2* transcripts.

947



948

949 **Figure S4.** Characterisation of INs by gene ontology analysis. Gene ontology (GO)  
950 analysis in IN5,8 (orange in A) versus all other cells (green in A) reveals enrichment  
951 of GO terms associated with (B) synaptic activity, maturation, and plasticity. (C)  
952 gradient plots of CAMK2, ADCY1 showing that these transcripts are most highly  
953 expressed in IN5,8.

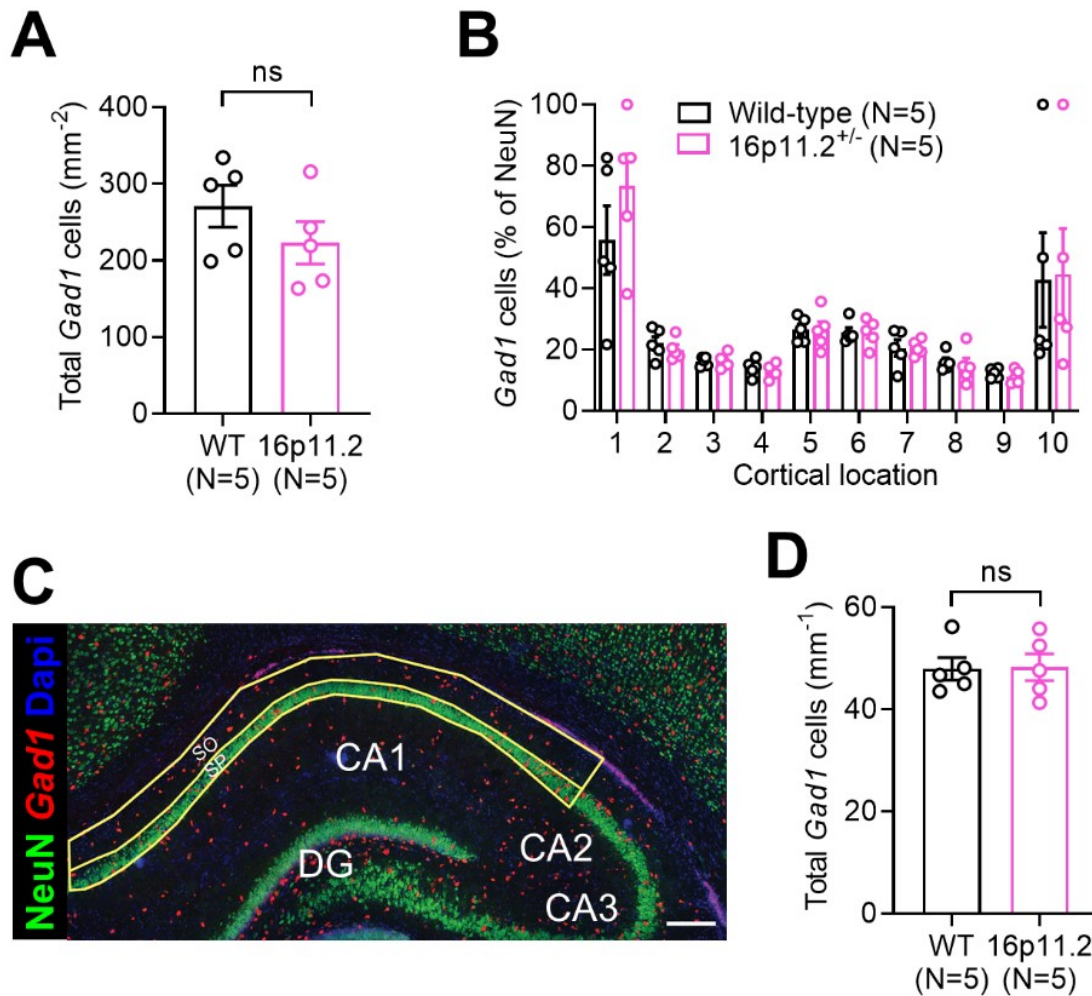
954

955

956

957

958



959

960 **Figure S5: No change in total IN number in somatosensory cortex or**  
961 **hippocampus of the *16p11.2*<sup>+/-</sup> rat. (A)** Based on the expression of *Gad1* mRNA,  
962 quantification of the total number of INs across the whole somatosensory column from  
963 WT (N=6) and *16p11.2*<sup>+/-</sup> (N=6) rats. **(B)** No change in the relative ratio of *Gad1*-  
964 positive cells to total neurons (NeuN) was observed within the cortical column. **(C)**  
965 Expanded view of CA1 of the hippocampus from the same image as in Figure 5A,  
966 showing *Gad1* in situ hybridisation (red), NeuN immunolabelling (green) and DAPI  
967 nuclei (blue). Regions used for cell counts in *str. pyramidale* (SP) and *str. oriens* (SO)  
968 are delineated with yellow lines. Scale bar: 200  $\mu$ m. **(D)** Total number of *Gad1*-positive  
969 neurons measured in CA1 from WT (N=5) and *16p11.2*<sup>+/-</sup> (N=5) rats. Statistics shown:  
970 ns –  $p > 0.05$  from Student's 2-tailed t-test.

971

972 **SUPPLEMENTARY TABLES**

973 **Table S1**

974

Parameter tested	SSt INs			CA1 pyramidal cells		
	Wild-type	16p11.2 <sup>+/-</sup>	<i>p</i>	Wild-type	16p11.2 <sup>+/-</sup>	<i>p</i>
n (N)	30 (15)	18 (13)		18 (10)	18(9)	
Resting membrane potential (mV)	-56.6 ± 1.5	-60.9 ± 1.8	0.25	-64.6 ± 1.9	-65.3 ± 1.1	0.88
Input resistance (MΩ)	204 ± 22	220 ± 26	0.65	113 ± 15	105 ± 18	0.73
Membrane time-constant (ms)	34.5 ± 5.3	34.9 ± 6.3	0.72	24.2 ± 1.7	23.0 ± 2.3	0.74
Membrane capacitance (pF)	162 ± 11	152 ± 16	0.30	239 ± 17	245 ± 16	0.97
Voltage sag (mV)	18.2 ± 1.7	17.9 ± 2.0	0.50	8.4 ± 0.6	9.4 ± 1.2	0.43
Sag (% of maximum)	32.9 ± 2.2	36.0 ± 3.7	0.76	23.9 ± 1.6	25.1 ± 1.5	0.65
Rheobase (pA)	233 ± 22	194 ± 28	0.11	256 ± 28	266 ± 20	0.71
Voltage threshold (mV)	-39.6 ± 0.7	-42.1 ± 0.9	<b>0.03</b>	-42.4 ± 1.3	-41.9 ± 1.0	0.41
AP amplitude (mV)	98.3 ± 3.2	97.7 ± 3.3	0.64	122.5 ± 1.8	119.8 ± 2.9	0.61
AP 20-80% rise-time (ms)	0.17 ± 0.01	0.16 ± 0.01	0.38	0.15 ± 0.01	0.16 ± 0.01	0.87
AP half-height duration (ms)	0.62 ± 0.02	0.61 ± 0.04	0.81	1.00 ± 0.02	0.98 ± 0.03	0.60
AP max. rise-rate (mV.ms <sup>-1</sup> )	276 ± 18	310 ± 22	0.48	455 ± 19	443 ± 29	0.96
AP max. decay-rate (mV.ms <sup>-1</sup> )	124 ± 7	139 ± 13	0.53	77 ± 1	79 ± 4	0.64
Peak firing (Hz)	54.8 ± 5.0	71.6 ± 7.9	<b>0.02</b>	30.3 ± 3.1	31.4 ± 1.8	0.70

975

976

977

978

979